Journal of Thermal Analysis and Calorimetry (2019) 138:1723–1743
https://doi.org/10.1007/s10973-019-08258-w

MHD natural convection of Cu–Al_2O_3 water hybrid nanofluids in a cavity equally divided into two parts by a vertical flexible partition membrane

M. Ghalambaz[1,2] · S. A. M. Mehryan[3] · E. Izadpanahi[4] · A. J. Chamkha[5,6] · D. Wen[1,7]

Received: 11 January 2019 / Accepted: 12 April 2019 / Published online: 2 May 2019

Abstract

The aim of the present study is to investigate the effects of a hybrid nanofluid in a square cavity that is divided into two equal parts by a vertical flexible partition in the presence of a magnetic field. A numerical method called the Galerkin finite element method is utilized to solve the governing equations. The effects of different parameters, namely the Rayleigh number ($10^6 \leq Ra \leq 10^8$) and the Hartmann number ($0.0 \leq Ha \leq 200$) as well as the effects of nanoparticles concentration ($0.0 \leq \varphi \leq 0.02$) and magnetic field orientation ($0 \leq \gamma \leq \pi$), on the flow and heat transfer fields for the cases of pure fluid, nanofluid and hybrid nanofluid are investigated. The results indicate that the streamline patterns change remarkably and the convective heat transfer augments with increasing values of the Rayleigh number. Additionally, the maximum stress imposed on the flexible partition resulting from the interaction of the partition and pure fluid is more than those caused by the nanofluid and the hybrid nanofluid. Furthermore, the increase in the magnetic field strength decreases the fluid velocity in the cavity, which declines the fluid thermal mixing and heat transfer effects.

Keywords Flexible membrane · Alumina–Copper nanoparticles · Hybrid nanofluid · Magnetic field · Natural convection

List of symbols

B_o Applied magnetic field
$\mathbf{d}_s$ Partition displacement-vector
E Young's modulus in dimensional form
E_τ Dimensionless elasticity modulus
$\mathbf{F}_v$ Vector of body force

✉ M. Ghalambaz
mohammad.ghalambaz@tdtu.edu.vn

✉ D. Wen
d.wen@buaa.edu.cn; d.wen@leeds.ac.uk

S. A. M. Mehryan
alal171366244@gmail.com

E. Izadpanahi
eizad001@fiu.edu

A. J. Chamkha
achamkha@pmu.edu.sa

[1] School of Aeronautic Science and Engineering, Beihang University, Beijing, People's Republic of China

[2] Department for Management of Science and Technology Development, Ton Duc Thang University, Ho Chi Minh City, Vietnam

[3] Young Researchers and Elite Club, Yasooj Branch, Islamic Azad University, Yasooj, Iran

[4] Department of Mechanical and Materials Engineering, Florida International University, Miami, FL 33174, USA

[5] Mechanical Engineering Department, Prince Mohammad Endowment for Nanoscience and Technology, Prince Mohammad Bin Fahd University, Al-Khobar 31952, Saudi Arabia

[6] RAK Research and Innovation Center, American University of Ras Al Khaimah, P.O. Box 10021, Ras Al Khaimah, United Arab Emirates

[7] School of Chemical and Process Engineering, University of Leeds, Leeds, UK

g	Gravity constant vector
L	Size of square cavity
P	Fluid pressure
Pr	Prandtl number
Ra	Rayleigh number in vector form
Ra	Rayleigh number
t	Time
T	Fluid temperature
x, y	Cartesian coordinates
u	Velocity vector
w	Velocity vector of the moving coordinates of the grids

Greek symbols

α	Thermal diffusivity
β	Thermal expansion coefficient
φ	Volume fraction of nanoparticles
γ	Angle of magnetic field orientation
σ	Tensor of stress in partition
χ	Magnetic permeability
τ	Non-dimensional time
ν	Fluid kinematic viscosity
υ	Poisson's ratio of the partition
ρ	Density
ρ_{R}	Density ratio of the fluid and the partition

Subscripts

c	Cold
f	Base fluid
h	Hot
hnp	Hybrid nanoparticles
hnf	Hybrid nanofluid
nf	Nanofluid
P	Partition
s	Solid

Superscripts

*	Dimensional parameters

Introduction

When it comes to enclosures, natural convection is the most important mean of heat transfer. Enclosures have a variety of applications in engineering such as boilers, energy storage and conservation systems, solar collectors–receivers, nuclear reactor systems, food and metallurgical industries, fire control and chemical, etc. Comprehensive studies have been done in recent years in this field [1–5]. Although, in many industrial applications, natural convection is considered as a beneficial phenomenon, the phenomenon becomes undesirable in some cases. One of the ways to control that is by applying an external magnetic field for magneto hydro dynamic (MHD) flows [6–11]. Results obtained by Sathiyamoorthy and Chamkha [7] indicated that the magnetic field with inclined angle affected the flow field and heat transfer rates. Sheikholeslami and Ganji investigated [12] natural convection heat transfer of ferrofluid Fe_3O_4–water nanofluid with a point source external magnetic field. Their results indicated the reduction in heat transfer caused by the magnetic field.

Additionally, the flow inside cavities could be controlled by inserting dividers [13, 14]. By using dividers inside cavities, the flow field, and correspondingly the heat transfer rate, can be controlled. The cavities with partitions can be classified in three groups: (a) partially divided cavities [15–17], (b) cavities with inclined partitions [18, 19] and (c) cavities fully divided horizontally or vertically with partition/partitions [20–22]. Jamesahar et al. [21] and Mehryan et al. [22] conducted a numerical study on the heat transfer in a divided square cavity using a flexible membrane. Jamesahar et al. [21] reported that the presence of a flexible diagonal partition could enhance the heat transfer, while the deflection of the flexible partition could also affect the heat and flow patterns. It was reported by Mehryan et al. [23] that there was an optimum value of magnetic inclination angle to maximize the heat transfer in the partitioned cavity. Additionally, they [23] reported that the dimensionless average temperature could be increased by applying the magnetic field when the Rayleigh number was in a moderate range ($Ra = 10^6$–10^7), especially under a magnetic field (Hartmann number $Ha \geq 50$). Xu et al. [24] studied the transient natural convection inside a differentially heated cavity, which was filled with water and separated by a solid partition without any deflection. Three categorized natural convection main stages were found, including an initial stage, a transitional stage and a steady-state stage.

Fully divided cavities with an impermeable divider have many interesting applications. For instance, thermal conductive partitions are used to divide a box containing electronic units, and a conductive metallic cover can be installed to separate a sensitive electronic equipment from the surrounding. Chemical species, in many cases, should be segregated from each other in a chemical reactor, but heat can be transferred between the species through partitions. These practical applications of fully divided cavities have motivated researchers to investigate the effect of dividers and partitions on convective heat and mass transfer phenomena in cavity enclosures. An experimental study has been done by Nishimura et al. [25] considering the effects of N multiple vertical partitions on natural convection in a rectangular enclosure. It was found that the Nusselt number decreased with the increase in the partition numbers.

The natural convection phenomena in a partitioned cavity were investigated by Oztop et al. [26]. On each sub-cavity, combinations of water and air were considered. Additionally, the effects of the presence of a vertical partition on the flow and heat inside in an enclosure were investigated by Kahveci [27], with the partition heated by uniform heat flux. It was shown that the vertical partition had a considerable effect on natural convection when the two parts of the enclosure were filled with the same fluid.

Dispersion of nanometer-sized particles in base fluids is now known as nanofluids, which are now widely used in a variety of thermal systems to enhance the heat transfer characteristics [28–33]. Even for a small volume fraction of nanoparticles, nanofluids have shown an extreme increase in their thermal conductivities. Fluids such as water, ethylene glycol, bio-fluids, polymer solutions, oils and other lubricants are usually considered as base fluids. Different types of nanoparticles including metallic particles (Cu, Al, Fe, Au, and Ag) and non-metallic particles (Al_2O_3, CuO, Fe_3O_4, TiO_2, and SiC) have been utilized in experimental and numerical studies. The non-metallic particles such as Al_2O_3 are known for their excellent stability and chemical inertness. Unfortunately, non-metallic particles show lower thermal conductivity compared to the metallic nanoparticles. Kahveci [34] investigated five types of nanoparticles inside a differentially heated, tilted enclosure, and showed that the average heat transfer rate of metallic nanoparticles was higher than those of non-metallic nanoparticles. On the other hand, metallic nanoparticles, for instance, copper (Cu) or aluminum (Al) have much higher thermal conductivities, but their poor stability and tendency to chemical reactions prevented researchers to utilize them widely.

Most of the earlier investigations have addressed the effect of using a single type of metallic or non-metallic nanoparticles on the heat transfer performance of nanofluids. However, combination of non-metallic nanoparticles with a small amount of metal nanoparticles can enhance the thermal properties of the base fluid significantly. Jena et al. [35] have successfully synthesized a homogeneous mixture of well-dispersed CuO and Al_2O_3 composite briquette by using hydrogen reduction technique. Suresh et al. [36] have investigated the thermos-physical properties of Alumina–Copper hybrid nanofluids. The outcomes demonstrated that the presence of hybrid nanoparticles significantly enhanced the thermal conductivity and dynamic viscosity of hybrid nanofluids. In an experimental study by Suresh et al. [37], it was reported that the Nusselt number can be increased up to 13.56% by using Al_2O_3–Cu hybrid nanofluids. Mahian et al. [38, 39] performed an excellent review on modeling and simulation of nanofluid flows. More studies on the hybrid nanofluid can be observed in [40–45].

The membranes are in important parts of fuel cells, filters and separators. Therefore, any approach capable of modeling or analysis of the membranes is of great importance. As mentioned, in very recent studies, Jamesahar et al. [21] and Mehryan et al. [23] have studied the heat transfer of a pure fluid in a square cavity divided into two sub-cavities by a flexible partition. Following [21] and [23], the present study aims to analyze the effects of Cu–Al_2O_3/water hybrid nanofluid and magnetic field on the natural convection inside a fully divided cavity. The motivation of the present study is to answer the following questions:

1. What is the effect of magnetic field inclination on the heat and flow patterns of hybrid nanofluids?
2. Does the presence of nanoparticles enhances the heat transfer in the divided cavity? Is there any significant difference between heat transfer enhancement of Al_2O_3 nanoparticles and Cu–Al_2O_3 hybrid nanoparticles?
3. How the presence of nanoparticles could change the shape of the flexible partition and the heat transfer rate?
4. Which types of nanoparticles (Al_2O_3 or Cu–Al_2O_3) are better for heat transfer enhancement in the presence of a magnetic field?

Description of the work

A view of the considered problem geometry is shown schematically in Fig. 1 which is utilized to derive the governing equations and boundary conditions. The dimensions of the enclosure in x^*, y^* coordinates are so

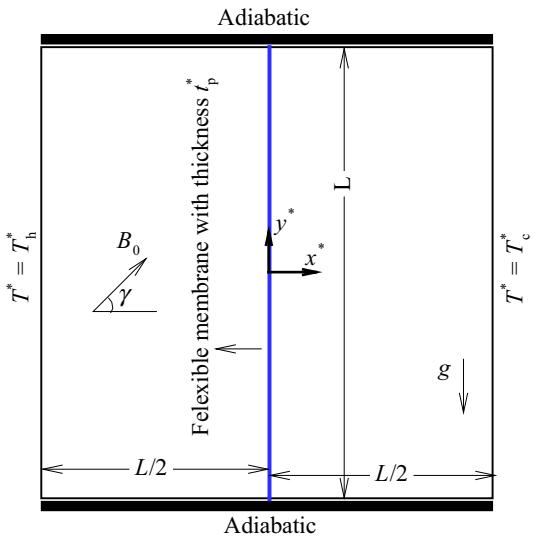

Fig. 1 The schematic view of the physical model and boundary conditions

Table 1 The thermophysical properties of the hybrid nanofluid components [46]

Physical properties	Water	Cu	Al_2O_3
C_p/J kg^{-1} K^{-1}	4179	385	765
k/W m^{-1} K^{-1}	0.613	401	40
α/m^2 s^{-1}	1.47×10^{-7}	1.11×10^{-4}	131.7×10^{-7}
β/K^{-1}	21×10^{-5}	1.67×10^{-5}	0.85×10^{-5}
ρ/kg m^{-3}	997.1	8933	3970
μ/kg m^{-1} s^{-1}	8.9×10^{-4}	–	–
χ/Ω m^{-1}	0.05	5.96×10^{7}	1×10^{-10}

much higher than that in z^* one. Accordingly, a two-dimensional mathematical domain is considered. It is defined that the left surface with the temperature of T_h^* is hotter than the right surface with the temperature of T_c^* ($T_h^* > T_c^*$). The lower and upper bounds of the enclosure are thermally impervious. Moreover, it is assumed that all the solid boundaries are made of electrically non-conducting material. A vertical thin flexible partition breaks up the square cavity into two equal parts. t_p^* represents the thickness of the flexible partition. The flexible partition material is isotropic and nonmagnetic. Both parts are glutted with the Newtonian electromagnetic Cu–Al_2O_3/water hybrid nanofluid or Al_2O_3/water nanofluid. A hybrid nanofluid contains a base fluid and two or more types of nanoparticles. In this study, solid particles of the hybrid nanofluid are the nanoparticles of Al_2O_3 and Cu. The thermophysical properties of the forming components of hybrid/regular nanofluid are represented in Table 1. Both the types of nanoparticles are always suspended and stable. This means that the nanoparticles do not agglomerate and become collective. There is a thermal and dynamic equilibrium between the suspended nanocomposite particles and the host fluid. The fluid flow is laminar and steady state. The buoyancy effects are modeled using Boussinesq approximation. Since the flexible partition is thin and with low thermal resistance, the gradient of temperature in it is zero. Additionally, all the solid surfaces are impervious to the mass flow. The flow domain is exposed a tilted magnetic field with the amplitude and angle of B_0 and γ, respectively. It is supposed that the convection and diffusion values of the energy balance are so much higher than viscous dissipation and Joule heating. The densities of the hybrid nanofluid and the flexible partition are the same. The partition behaves as a hyper-elastic material reacting nonlinearly against applied loads.

The Lorentz force is one that is applied to the flow domain due to the existence of the magnetic field vector **B** with the density of electrical current **J**

$$\mathbf{LF} = \mathbf{J} \times \mathbf{B} \tag{1a}$$

where **J** is defined by Ohm's law:

$$\mathbf{J} = \chi_{hnf}(-\nabla\phi + \mathbf{u}^* \times \mathbf{B}) \tag{1b}$$

where χ_{hnf} represents the electrical conductivity of the fluid. $\mathbf{u}^*(u^*, v^*)$ is the velocity vector of the fluid in the cavity. The bounds of the enclosure are electrically impervious, so, according to the Maxwell theory, $\nabla\phi = 0$. Therefore, we have

$$\mathbf{LF} = \chi_{hnf}(\mathbf{u}^* \times \mathbf{B}) \times \mathbf{B} \tag{1c}$$

Description of the reciprocal effects of the fluid and deformable solid material is performed by the known technique of the Arbitrary Lagrangian–Eulerian (ALE). The fluid flow within the enclosure is portrayed by the incompressible mass conservation and the linear momentum equations for the pressure and velocity fields [21, 23, 47]:

$$\nabla^* \cdot \mathbf{u}^* = 0 \tag{2}$$

$$\frac{\partial \mathbf{u}^*}{\partial t} + (\mathbf{u}^* - \mathbf{w}^*) \cdot \nabla^* \mathbf{u}^* = -\frac{1}{\rho_{hnf}} \nabla^* P^* + \frac{\mu_{hnf}}{\rho_{hnf}} \nabla^{*2} \mathbf{u}^* + \frac{\chi_{hnf}}{\rho_{hnf}} (\mathbf{u}^* \times \mathbf{B}) \times \mathbf{B} + \beta_{hnf} \mathbf{g} (T^* - T_c^*) \tag{3}$$

$$\frac{\partial T^*}{\partial t} + (\mathbf{u}^* - \mathbf{w}^*).\nabla^* T^* = \alpha_{hnf} \nabla^{*2} T^* \tag{4}$$

The structural deformations of the flexible partition can be achieved by the following nonlinear geometric and elastic formulation:

$$\rho_s \frac{d^2 \mathbf{d}_s^*}{dt^2} - \nabla^* \boldsymbol{\sigma}^* = \mathbf{F}_v^* \tag{5}$$

$\mathbf{F}_v^*$ of the above-written equation is the applied volume forces on the deformable partition, $\boldsymbol{\sigma}^*$ is the solid stress tensor, $\mathbf{d}_s^*$ the displacement vector of moving coordinate system so that $d\mathbf{d}_s^*/dt = \mathbf{w}^*$ and ρ_s is the density of the partition.

In this study, the stress tensor $\boldsymbol{\sigma}^*$ is computed using a Neo-Hookean model to characterize the stress–strain nonlinear behavior of a hyper-elastic material with large deformations. The hyper-elastic theory is used more for modeling of rubbery behavior of a polymeric material and polymeric foams that can have large deformations. The model can be written as follows:

$$\boldsymbol{\sigma}^* = J^{-1} F S F^{\mathrm{T}} \tag{6}$$

where

$$F = \left(I + \nabla^* \mathbf{d}_s^*\right), J = \det(F) \text{ and } S = \partial W_s / \partial \varepsilon \tag{7}$$

are the deformation gradient, determinant of the matrix F and the partial differential of the density function of strain

energy, respectively. Also, the density function of the strain energy W_s and strain ε is defined through the equations below:

$$W_s = \frac{1}{2}\mu_l\left(J^{-1}I_1 - 3\right) - \mu_l \ln(J) + \frac{1}{2}\lambda(\ln(J))^2 \tag{8}$$

$$\varepsilon = \frac{1}{2}\left(\nabla^* \mathbf{d}_s^* + \nabla^* \mathbf{d}_s^{*\mathrm{T}} + \nabla^* \mathbf{d}_s^{*\mathrm{T}} \nabla^* \mathbf{d}_s^*\right) \tag{9}$$

where

$$\lambda = Ev/((1+v)(1-2v)), \mu_l = E/(2(1+v)) \tag{10}$$

λ and μ_l of the above equations, known as Lame's first and second constants, respectively. I_1 is called the first constant of the deformation tensor.

All the bounds of the enclosure are motionless ($u^* = v^* = 0$). The lower and topper bounds of the both sub-cavities are thermally insulated ($\partial T^*/\partial y^* = 0$). The right hand wall is at the low temperature of $T^* = T_c^*$, while the temperature of the opposite wall is higher (i.e. $T^* = T_h^*$).

Along the fluid–solid interface, continuity of the dynamic motion and kinematic forces are the boundary conditions utilized to model the fluid and deformable divider interaction. These conditions can be represented as:

$$\frac{\partial \mathbf{d}_s^*}{\partial t} = \mathbf{u}^* \quad \text{and} \quad \boldsymbol{\sigma}^*.n = -P^* + \mu_f \nabla^* \mathbf{u}^* \tag{11}$$

Applying the conservation of energy on the flexible divider along with the previous assumptions results in the equation below:

$$\frac{\partial T^{*+}}{\partial n} = \frac{\partial T^{*-}}{\partial n} \quad \text{and } T^{*+} = T^{*-} \tag{12}$$

In this equation, the plus and minus marks denote the right and left sides of the deformable divider, respectively. Also, the boundary condition for both eyelets can be represented as follows:

$$[-P^* + \mu_{hnf} \nabla \mathbf{u}^*].n = 0 \tag{13}$$

To provide with dimensions, non-dimensional parameters are introduced below;

$$\begin{aligned}
&\mathbf{d}_s = \frac{\mathbf{d}_s^*}{L}, \boldsymbol{\sigma} = \frac{\boldsymbol{\sigma}^*}{E}, \tau = \frac{t\alpha_f}{L^2}, (x,y) = \frac{(x^*,y^*)}{L},\\
&\mathbf{u} = \frac{\mathbf{u}^* L}{\alpha_f}, \mathbf{w} = \frac{\mathbf{w}^* L}{\alpha_f}\\
&P = \frac{L^2}{\rho_f \alpha_f^2} P^*, T = \frac{T^* - T_c^*}{T_h^* - T_c^*}, \nabla = \frac{\nabla^*}{1/L}, \nabla^2 = \frac{\nabla^{*2}}{1/L^2},\\
&t_p = \frac{t_p^*}{L}
\end{aligned} \tag{14}$$

To dimensionalize the equations, the above parameters are substituted for the Eqs. (1)–(4). Therefore, we then have,

$$\frac{1}{\rho_R}\frac{\mathrm{d}^2 \mathbf{d}_s}{\mathrm{d}\tau^2} - E_\tau \nabla \boldsymbol{\sigma} = E_\tau \mathbf{F}_v \tag{15}$$

$$\nabla.\mathbf{u} = 0 \tag{16}$$

$$\begin{aligned}
\frac{\partial \mathbf{u}}{\partial \tau} + (\mathbf{u} - \mathbf{w}) \cdot \nabla \mathbf{u} = &-\frac{\rho_f}{\rho_{hnf}} \nabla P + \left(\frac{\rho_f}{\rho_{hnf}}\right)\left(\frac{\mu_{hnf}}{\mu_f}\right) Pr \nabla^2 \mathbf{u}\\
&+ \frac{(\rho\beta)_{hnf}}{\rho_{hnf}\beta_f} PrRaT\\
&+ \left(\frac{\rho_f}{\rho_{hnf}}\right)\left(\frac{\chi_{hnf}}{\chi_f}\right) Pr(\mathbf{u} \times \mathbf{Ha}) \times \mathbf{Ha}
\end{aligned} \tag{17}$$

$$\frac{\partial T}{\partial \tau} + (\mathbf{u} - \mathbf{w}).\nabla T = \frac{\alpha_{hnf}}{\alpha_f} \nabla^2 T \tag{18}$$

In Eq. (15), ρ_R is the density ratio, E_τ is the dimensionless elasticity modulus and $\mathbf{F}_v$ is dimensionless volume force vector.

$$\rho_R = \frac{\rho_{hnf}}{\rho_s}, E_\tau = \frac{EL^2}{\rho_{hnf}\alpha_f^2}, \mathbf{F}_v = \frac{(\rho_{hnf} - \rho_s)L\mathbf{g}}{E} \tag{19}$$

In Eq. (17), the dimensionless numbers are defined as the following:

$$Pr = \frac{\upsilon_f}{\alpha_f}, Ra = \frac{g\beta(T_h - T_c)L^3}{\upsilon_f \alpha_f}, \mathbf{Ha} = L\mathbf{B}\sqrt{\frac{\chi_f}{\mu_f}} \tag{20}$$

The non-dimensional parameter of Hartmann number is a vector with two components along the x- ($Ha \sin(\gamma)$) and the y-axes ($Ha \cos(\gamma)$). The volume force expression rising from the magnetic field, known as Lorentz force, is rewritten as follows:

In the x-direction:

$$\left(\frac{\rho_f}{\rho_{hnf}}\right)\left(\frac{\chi_{hnf}}{\chi_f}\right) PrHa^2(v \sin\gamma\cos\gamma - u\sin^2\gamma) \tag{21}$$

In the y-direction:

$$\left(\frac{\rho_f}{\rho_{hnf}}\right)\left(\frac{\chi_{hnf}}{\chi_f}\right) PrHa^2(u \sin\gamma\cos\gamma - v\cos^2\gamma) \tag{22}$$

where

$$\rho_{hnf} = \rho_f\left(1 - \varphi_{hnp}\right) + \rho_{Al_2O_3}\varphi_{Al_2O_3} + \rho_{Cu}\varphi_{Cu} \tag{23}$$

$$(\rho\beta)_{hnf} = (1 - \varphi_{hnp})(\rho\beta)_f + \varphi_{Al_2O_3}(\rho\beta)_{Al_2O_3} + \varphi_{Cu}(\rho\beta)_{Cu} \tag{24}$$

$$\chi_{hnf} = \chi_f\left(1 + \frac{3\left(\frac{\chi_{hnp}}{\chi_f} - 1\right)\varphi_{hnp}}{\left(\frac{\chi_{hnp}}{\chi_f} + 2\right) - \left(\frac{\chi_{hnp}}{\chi_f} - 1\right)\varphi_{hnp}}\right) \tag{25}$$

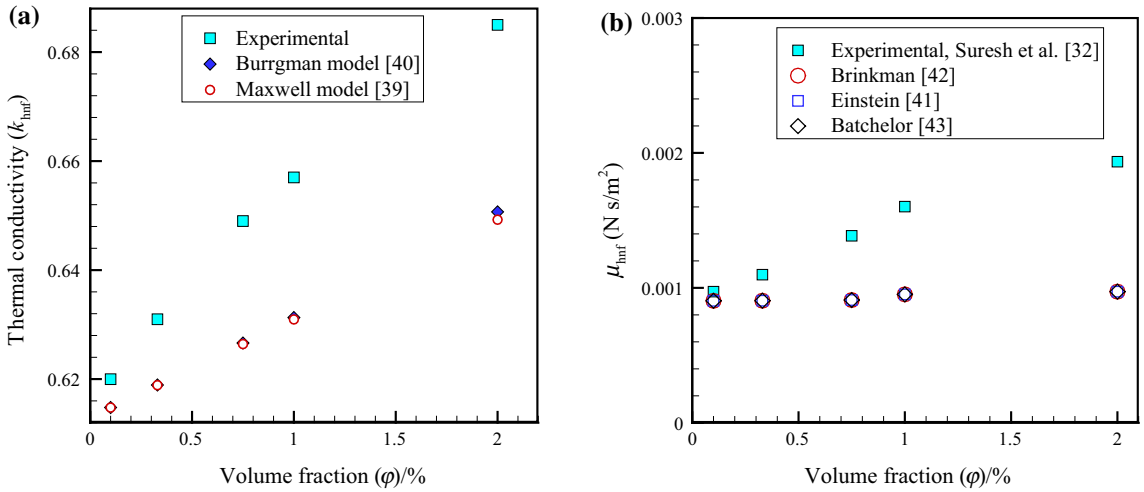

Fig. 2 **a** Thermal conductivity and **b** dynamic viscosity obtained by the classical models

$$\begin{aligned} \varphi_{hnp} &= \varphi_{Al_2O_3} + \varphi_{Cu} \\ \sigma_{hnp}\varphi_{hnp} &= \sigma_{Al_2O_3}\varphi_{Al_2O_3} + \sigma_{Cu}\varphi_{Cu} \end{aligned} \tag{26}$$

In all the above-mentioned relations, φ represents the nanoparticles concentration. here $\rho_s = \rho_{hnf}$, therefore the volume force of $\mathbf{F}_v$ is zero. Noticing the thermophysical properties represented in Table 1, the electrical conductivity orders of Al_2O_3 and Cu nanoparticles are O (10^{-10}) and O (10^7), respectively. Hence, compared to the nanoparticles of Cu, the electrical conductivity of Al_2O_3 nanoparticles is very close to zero. Therefore, the electrical conductivity of the hybrid nanoparticles can be rewritten as follows:

$$\chi_{hnp} = \left(\frac{\varphi_{Cu}}{\varphi_{hnp}}\right)\chi_{Cu} \tag{27}$$

The heat capacity of the hybrid nanofluid is calculated from the following equation:

$$(\rho c_p)_{hnf} = (1-\varphi_{hnp})(\rho c_p)_f + \varphi_{Al_2O_3}(\rho c_p)_{Al_2O_3} + \varphi_{Cu}(\rho c_p)_{Cu} \tag{28}$$

In addition, by employing the classical Maxwell [48] and Bruggeman [49] models, we then have:

The classical Maxwell model Maxwell [48]:

$$\frac{k_{hnf}}{k_f} = \frac{k_{hnp} + 2k_f - 2\varphi_{hnp}(k_f - k_{hnp})}{k_{hnp} + 2k_f + \varphi_{hnp}(k_f - k_{hnp})} \tag{29}$$

The classical Bruggeman model [49]:

$$k_{hnf} = \frac{1}{4}\left[(3\varphi_{hnp}-1)k_{hnp} + (2-3\varphi_{hnp})k_f\right] + \frac{k_f}{4}\sqrt{\Xi} \tag{30}$$

$$\begin{aligned} \Xi = \Bigg[&(3\varphi_{hnp}-1)^2\left(\frac{k_{hnp}}{k_f}\right) + (2-3\varphi_{hnp})^2 \\ &+2\left(2+9\varphi_{hnp}-9\varphi_{hnp}^2\right)\left(\frac{k_{hnp}}{k_f}\right)\Bigg] \end{aligned} \tag{31}$$

where in both of the above relations k_{hnp} is defined as:

$$k_{hnp}\varphi_{hnp} = k_{Al_2O_3}\varphi_{Al_2O_3} + k_{Cu}\varphi_{Cu} \tag{32}$$

In order to check the validity of these relations for Cu–Al_2O_3/water hybrid nanofluid, the values of the thermal conductivity obtained from both of the above relations for the hybrid nanofluid are calculated for different volume concentrations. Then, these values have been evaluated using the experimental data as shown in Fig. 2a. This comparison clearly depicts that the Maxwell and Bruggeman relations cannot estimate the real values of the thermal conductivity of the Cu-Al_2O_3/water hybrid nanofluid. Therefore, the remaining calculations are done based on the experimental thermal conductivity. Also, a comparison is done between the theoretical models and the experimental results to study the potential of the classical models to estimate the viscosity of the hybrid nanofluid. Three theoretical models are as follows:

Einstein model [50]:

$$\frac{\mu_{hnf}}{\mu_f} = 1 + k_{\mu 1}\varphi_{hnp} \tag{33}$$

Brinkman model [51]:

$$\frac{\mu_{hnf}}{\mu_f} = \frac{1}{(1-\varphi_{hnp})^{2.5}} \tag{34}$$

Batchelor model [52]:

$$\frac{\mu_{hnf}}{\mu_f} = 1 + k_{\mu 1}\varphi_{hnp} + k_{\mu 2}\varphi_{hnp}^2 \tag{35}$$

Table 2 The thermal conductivity and dynamic viscosity obtained by experiment [36]

φ_{hnp}/%	φ_{Cu}/%	$\varphi_{Al_2O_3}$/%	k/W m^{-1} K^{-1}	$\mu \times 10^3$/kg m^{-1} s^{-1}
0.1	0.0038	0.0962	0.619982	0.972
0.33	0.0125	0.3175	0.63098	1.098
0.75	0.0285	0.7215	0.649004	1.386
1	0.038	0.962	0.657008	1.602
2	0.0759	1.9241	0.684992	1.935
0.1	0	0.1	0.614055	0.9041
0.33	0	0.33	0.6190041	0.9049
0.75	0	0.75	0.6309797	0.9098
1	0	1	0.6437496	0.95184
2	0	2	0.6571916	0.972

As this comparison shows in Fig. 2b, the classical models significantly underpredict the viscosity. For this reason, the experimental results are employed to continue the computations. The experimental thermal conductivity and dynamic viscosity of Al_2O_3/water nanofluid and Cu–Al_2O_3/water hybrid nanofluid are given in Table 2. Table 2 also shows the volume fractions of both the nanoparticles Cu and Al_2O_3 suspended in the basefluid.

The dimensionless forms of the boundary conditions are:

For all the out bounds $u = v = 0$

For the adiabatic walls at the top and bottom $\dfrac{\partial T}{\partial y} = 0$ (36a)

For the left bound $T = 1$

For the right bound $T = 0$ (36b)

For the partition $\dfrac{\partial T^+}{\partial n} = \dfrac{\partial T^-}{\partial n}$ and $T^+ = T^-$ (36c)

On the solid-fluid interface: $\dfrac{\partial \mathbf{d}_s}{\partial \tau} = \mathbf{u}$ and $E_\tau \boldsymbol{\sigma}.n$

$$= -P + \left(\frac{\mu_{hnf}}{\mu_f}\right) Pr \nabla \mathbf{u} \tag{37}$$

For the eyelets:

$$\left[-P + \left(\frac{\mu_{hnf}}{\mu_f}\right) Pr \nabla \mathbf{u}\right].n = 0 \tag{38}$$

The local heat transfer rate is defined by the following relation:

$$Nu_{local} = -\frac{k_{hnf}}{k_f}\frac{\partial T}{\partial x} \tag{39}$$

Integrating the above relation leads to the mean Nusselt number:

$$Nu_{avg} = \int_0^1 Nu_{local} dy \tag{40}$$

Another important parameter is the mean temperature of the whole domain:

$$T_{avg} = \frac{\int_A T_{local} dA}{\int_A dA} \tag{41}$$

Solution procedure, grid evaluation and verification

Since the system of the governing Eqs. (15)–(18) as well as the boundary conditions (36)–(38) are coupled and non-linear, it is necessary to use a numerical method to solve them. To do this, the numerical Galerkin finite element approach is applied to do the weak form of the equations in the deformable grid system of ALE. The details of the Galerkin finite element approach have been explained in [44]. Fluid and solid are two regions of the computational domain. Both the regions are discretized to small structural elements. Before starting calculations, to evaluate the solution sensitivity to the element numbers, the grid independence test is done. The gird used is non-uniform structural quadrilateral grid. This test is performed for the case $Ra = 10^8$, $Ha = 0$, $\varphi_{hnp} = 0$ and $E_\tau = 10^{14}$. The results of the examination are presented in Fig. 3 and Table 3. The figure and table are made based on Nu_{local} and ψ_{max}, respectively. ψ is the stream function. Figure 3 shows that the variations of Nu_{local} are so slight when the number of elements is more than 50 × 50. However, as it is shown in Table 3, the relative error is 15.40% for this grid. So, it is necessary to evaluate the grids with the more number of

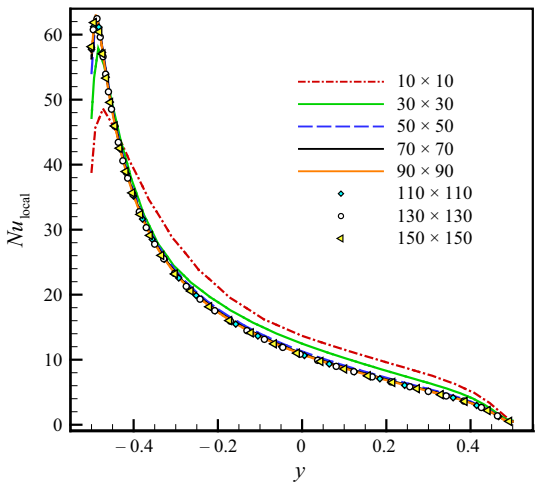

Fig. 3 Grid independence test in $Ra = 10^8$, $\varphi_{hnp} = 0$ and $Ha = 0$

Table 3 The grid independence test based on the maximum values of streamlines

Elements	10 × 10	30 × 30	50 × 50	70 × 70	90 × 90	110 × 110	130 × 130	150 × 150
$\|\psi\|_{max}$	64.05	52.68	44.57	42.35	41.51	41.08	40.85	40.70
*Error		17.75	15.40	4.98	1.99	1.02	0.58	0.36

*Error = 100 × ($|\psi|_{max,i+1}$ − $|\psi|_{max-i}$ in the present grid size)/$|\psi|_{max,i+1}$

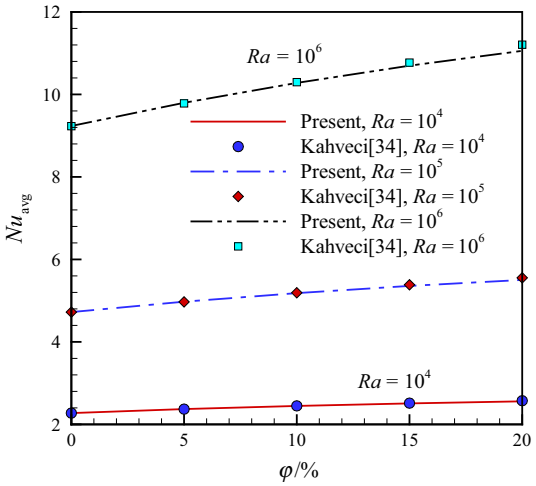

Fig. 4 Variations of Nu_{avg} according to the nanoparticles concentration φ at the various values of Ra resulted from [34] and the present study

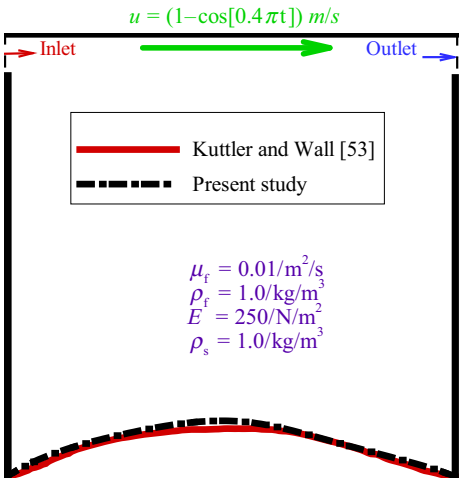

Fig. 5 The deformation curves of the deformable lower bound of the lid-driven enclosure examined by Küttler and Wall [53] and the present study at t = 7.5 s

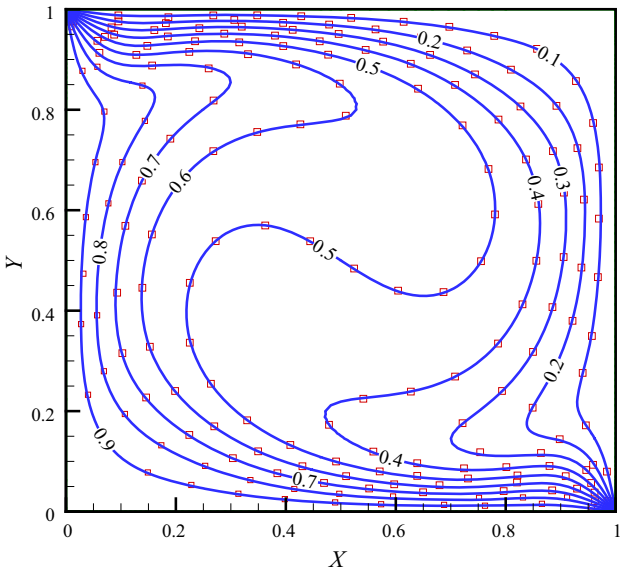

Fig. 6 The isotherms of this study (solid lines) and those obtained by Sathiyamoorthy and Chamkha [7] (points) for the case of a simple cavity when Ha = 10, Ra = 10^5, Pr = 0.054 and γ = 0

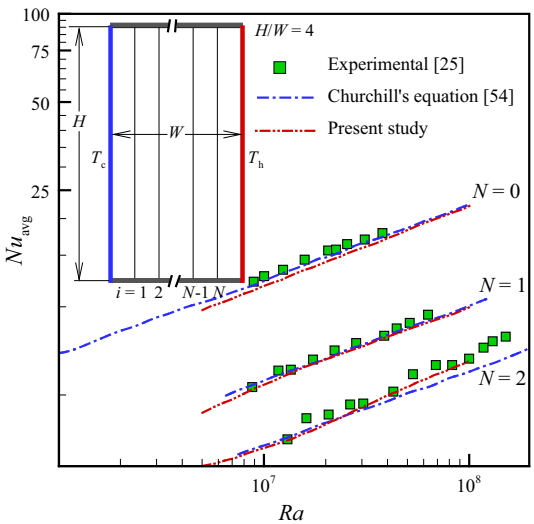

Fig. 7 The comparison of the results obtained by the present study with experimental data [25] and Churchill's relation [54] at AR=4 and Pr = 6

elements. The elements rising process continues until the relative error becomes < 1% (exactly 0.58%) in the grid 130 × 130. Therefore, the grid 130 × 130 is considered very appropriate and is chosen.

In the current investigation, several comparisons are performed to confirm the correctness and precision of the used numerical approach. The first validation consists of the case investigated in [34]. This comparison is shown in Fig. 4. The very high accordance between the results published by Kahveci [34] and those obtained by the

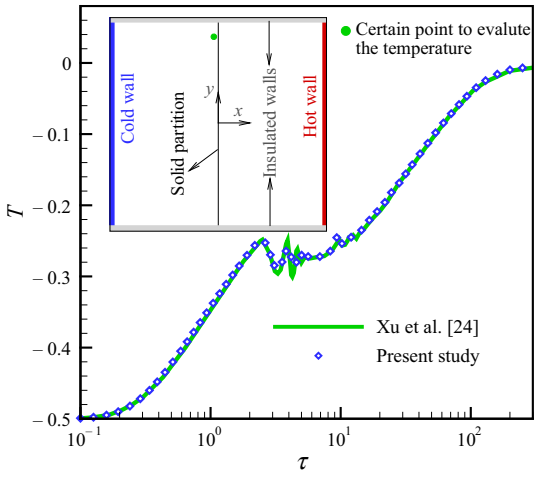

Fig. 8 Comparison of the dimensionless temperature reported by Xu et al. [24] and this study at the certain point (0.0083, 0.375)

present study vouches the correctness and precision of the numerical approach.

In the second validation (shown in Fig. 5), the curvature of the lower bound in the lid-driven cavity modeled by the present study and Küttler and Wall [53] are compared. The deformation curves simulated in this study and literature [53] are in a good agreement. Therefore, we can claim that the numerical procedure used is absolutely true.

The third validation is presented in Fig. 6 and shows the isotherms contours simulated in the current investigation and Sathiyamoorthy and Chamkha [7]. The good agreement between the outcomes of this investigation and those of Sathiyamoorthy and Chamkha [7] states that the employed solution method can correctly simulate a cavity under an external volume force.

As shown in Fig. 7, there exists an excellent compatibility for the numerical results rising from the current survey, experimental data of literature [25] and Churchill's equation [54]. Therefore, the used code is trusty. N is the number of vertical partitions dividing the enclosure. AR is the ratio of the height to width of the enclosure.

In the last validation, the precision and correctness of our data have been measured with those of Xu et al. [24]. These authors have studied the transient natural convection in a partitioned cavity subject to temperature difference at the side walls. Considering a very rigid partition and assuming zero fraction of nanoparticles, the results of the present study can be compared with the results reported in [24]. Figure 8 depicts a comparison between the results of the present study and [24] for the transient non-dimensional temperature profile. The non-dimensional temperature profile of Fig. 8 corresponds to a specified point with the coordinate of (0.0083, 0.375) which is located next to the partition. It is worth noticing that Xu et al. [24] have used $\tau = t\alpha Ra^{1/2}/L^2$ as the non-dimensional time variable.

The definition of the dimensionless time in the present investigation and Xu et al. [24] is different. The dimensionless time and Rayleigh number are defined as $\tau = t\alpha_f Ra^2/L^2$ and

$$Ra = g\beta\left(T_h^* - T_c^*\right)L^3/\upsilon_f\alpha_f$$

in the study of Xu et al. [24]. As can be seen from Fig. 8, there is an excellent agreement between the outcomes of this work and those reported in [24]. This validation verifies the sufficiency of the present formulation and solution to simulate the transient natural convection in the fluid domain and the partition.

Results and discussion

This section deals with the results acquired from the problem simulation. Here, the impacts of the dimensionless parameters like the Rayleigh number ($10^6 \le Ra \le 10^8$), nanoparticles concentration ($0.0 \le \varphi \le 0.02$), Hartmann number ($0.0 \le Ha \le 200$) and the angle of magnetic field vector ($0 \le \gamma \le \pi$) on the flow and temperature fields are investigated. Additionally, the effects of these parameters on the stresses of the flexible partition are studied. The values of $E_\tau = 10^{14}$ and $Pr = 6.2$ are kept constant. As previously mentioned, the densities of the hybrid nanofluid and the flexible partition are the same. Therefore, ρ_R and $\mathbf{F}_v$ have the value of 1 and 0, respectively. The angles rang of the magnetic field vector has been selected from 0 to π because the Lorentz force is a periodic one with the period of π.

Figure 9 depicts the streamlines for different values of nanoparticles concentration at low Rayleigh number 10^6 and high Rayleigh number 10^8. Here, Ha is 50 and γ is $2\pi/3$. Solid and dashed lines have been defined for the pure fluid and nanofluid, respectively. For both low and high Rayleigh numbers 10^6 and 10^8, the results illustrate that the presence of the Al_2O_3 nanoparticles enhances the strength of fluid flow while the simultaneous presence of Cu and Al_2O_3 nanoparticles reduces the flow strength. Moreover, it is observed that the governing streamlines patterns do not change by the presence of Cu–Al_2O_3 and Al_2O_3 nanoparticles; however, the nanoparticles can change the initial location of the streamlines.

Figure 10 illustrates the corresponding isotherms contours of the streamlines shown in Fig. 9 for both nanofluid and hybrid nanofluid. As Fig. 10(I) and (II)-(a) show, adding Al_2O_3 nanoparticles to the host fluid does not affect the temperature field. Dispersing the nanoparticles of Cu–

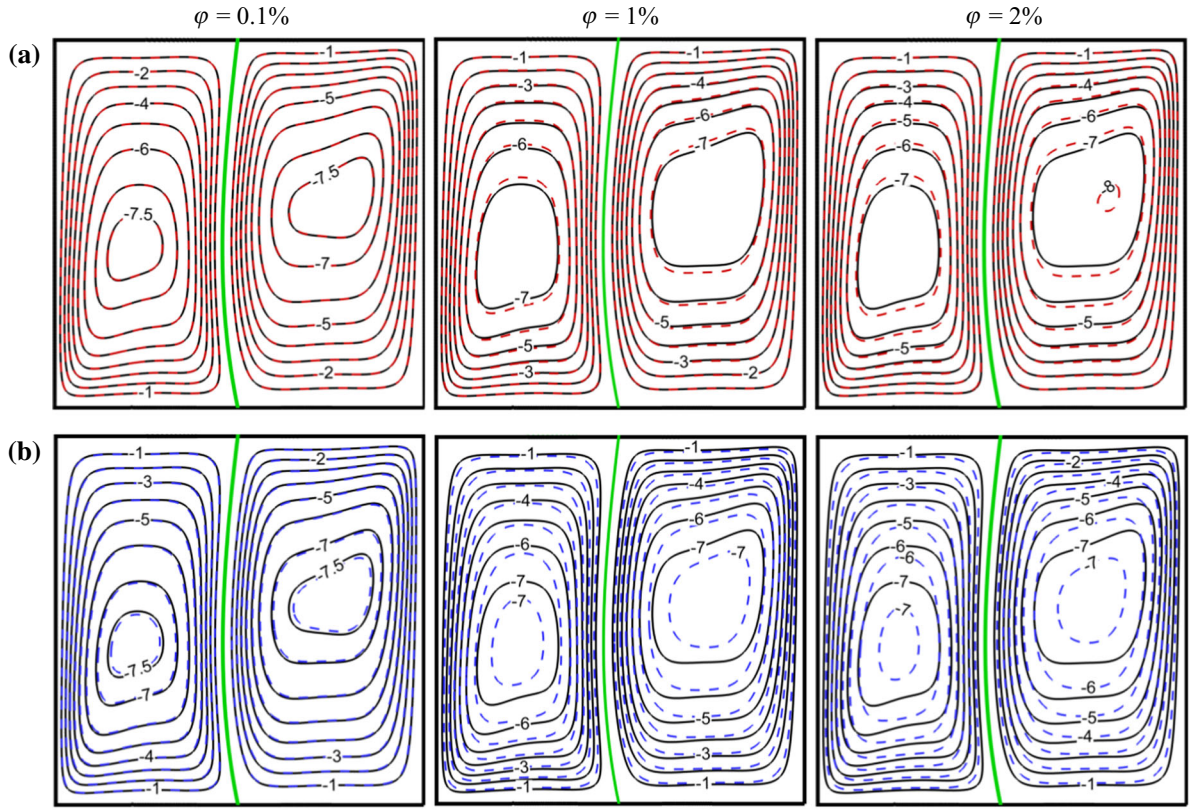

(I) $Ra = 10^6$

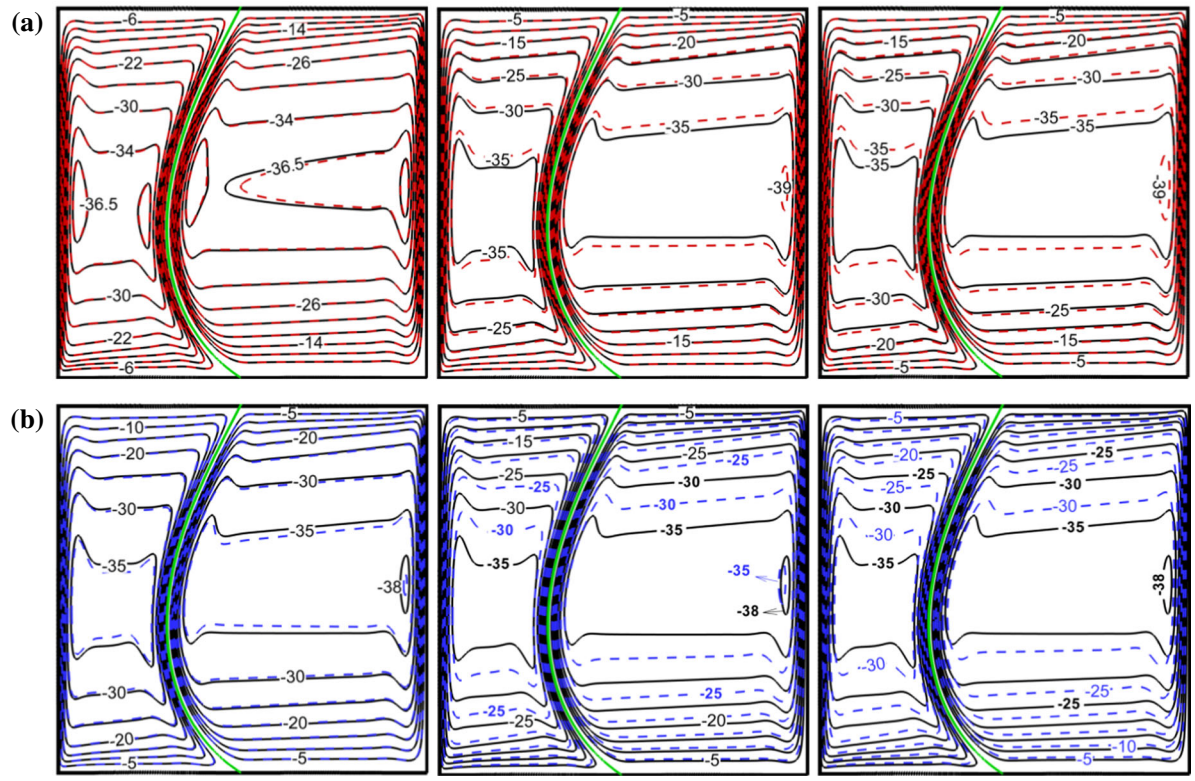

(II) $Ra = 10^8$

◀**Fig. 9** The streamlines contours of **a** Cu-Al_2O_3/water hybrid nanofluid (dashed line) and **b** Al_2O_3/water nanofluid (dashed line) for the various values of φ when **I** $Ra = 10^6$ and **II** $Ra = 10^8$ for the fixed values of $\gamma = 2\pi/3$ and $Ha = 50$

Al_2O_3 changes the location of the isotherms when $Ra = 10^6$ and $\varphi_{hnf} = 0.01$ and 0.02.

The impacts of Rayleigh and Hartmann numbers on the stream patterns are displayed in Fig. 11 for the picked values of $\gamma = \pi/6$ and $\varphi_{nf} = \varphi_{hnf} = 0.02$. As it is observed, increasing *Ra* significantly changes the stream patterns. The streamlines are horizontally stretched inside the cold sub-cavity with an increase in *Ra*. In addition, an increase in fluid flow strength due to the increase in *Ra* augments the flexible partition displacement. In some cases, the streamlines continue to stretch with increasing *Ra* until the vortices inside the cold sub-cavity break up into two vortices.

The strength of the vortices created in both the sub-cavities decreases with increasing *Ha*. The Lorentz force coming from the magnetic field is a drag force acting against the fluid movement. In fact, the magnetic field behaves as an opposite factor to the buoyancy force. Thus, it is justified that the fluid flow strength declines with an increase in *Ha*. Furthermore, it can be seen that the magnetic field has no effect on the flexible partition deformation at the steady state. In the cases with two or three vortices, an increase in the Hartmann number causes the vortices to approach to each other so that a unique vortex is finally formed. The center of the vortices in the left and right sub-enclosures swing toward down and up, respectively. The results state that in the similar conditions, the fluid flow strength for the single nanofluid (Al_2O_3/water nanofluid) is more than that of the hybrid nanofluid. Apparently, the reduction in the hybrid nanofluid flow strength is due to the intense increase in the hybrid nanofluid viscosity as a result of the simultaneous presence of Cu and Al_2O_3 nanoparticles.

Figure 12 shows the isotherms contours relating to the streamlines shown in Fig. 11. These results illustrate that the dominant mechanism of heat transfer varies with the change of Rayleigh number and Hartmann number. The isotherms incline to possess a stratification pattern as *Ra* augments. In fact, these stratification patterns are formed as a result of the increase in the fluid flow strength. The patterns demonstrate the thermal mixing of fluid. On the other hand, the lines of isotherms contours tend to be parallel to the vertical bounds when *Ha* increases. In other words, as the magnetic field strength augments, the conduction and advection contributions at heat transfer process increases and decreases, respectively. The isotherms of $Ha = 200$ and $Ra = 10^6$ clearly illustrate that the conduction mode is dominant.

Figure 13 depicts the effects of the parameters of magnetic field on the streamlines of the hybrid and single nanofluids. The values of *Ra* and φ are 10^7 and 0.02, respectively. Obviously, the strength of circulation augments as the angle of the magnetic field inclination, γ, grows by $\pi/2$. After that, the mobility of the fluid flow continuously begins to diminish when γ varies from $\pi/2$ to π. In fact, the vertical component of Lorentz force, which acts as a resistant one against buoyancy term, is reduced as γ increases from $\pi/2$ to π. This component of Lorentz force is exactly zero when $\gamma = \pi/2$. Therefore, it is expected that the buoyancy force has the maximum effects when the magnetic field vector is perpendicular with respect to the horizontal axis. In addition, the variations of inclination angle γ affect the governing patterns. The sub-figures shown in Fig. 13 depict that the created secondary vortices in the center of the sub-cavities unify with increasing *Ha* for all the inclination angles expect $\gamma = \pi/2$. This phenomenon is due to that the drag force of Lorentz has the least impact when it is applied perpendicularly. Furthermore, it can be seen that the results are the same for $\gamma = 0$ and π. As previously mentioned, the Lorentz force is a periodic one with the period of π.

The effect of γ and *Ha* on the isotherms is displayed in Fig. 14 for $Ra = 10^7$ and $\varphi_{hnf} = \varphi_{Al_2O_3} = 2\%$. When the magnetic field is applied to the flow domain, the fluid thermal mixing is reduced. When $Ra = 10^7$ and $\varphi_{hnf} = \varphi_{Al_2O_3} = 2\%$, it is not observed noticeable differences among the isotherms patterns. However, it is worth mentioning that the isotherms of $\gamma = \pi/2$ differ from those of the other values of γ.

Figure 15a, b shows the variations trend of Nu_{avg} according to γ for different values of *Ha*. The other parameters are constant so that $Ra = 10^8$ and $\varphi = 2\%$. Nu_{avg} increases as γ increases by $\gamma = \pi/2$. After that, it begins to reduce by $\gamma = \pi$. In other words, the maximum value of Nu_{avg} is at $\gamma = \pi/2$. This result arises from the fact that the fluid flow strength is maximum when $\gamma = \pi/2$. In addition, Nu_{avg} decreases with the increment of *Ha*. As said earlier, the mobility of the fluid flow exposed the magnetic field is reduced. Thus, this can justify that an increase in *Ha* causes a decrease in Nu_{avg}. Finally, the results depict that dispersing Al_2O_3 nanoparticles in the host fluid augments the rate of heat transfer, while Cu–Al_2O_3 nanoparticles decline the rate.

Figure 16a, b illustrates the variations trend of the mean temperature according to γ for different values of *Ha*. Here, φ and *Ra* are 0.02% and 10^8, respectively. The results indicate that T_{avg} reduces as γ augments. The T_{avg} variation according to γ is a quasi-sinusoidal function. Furthermore,

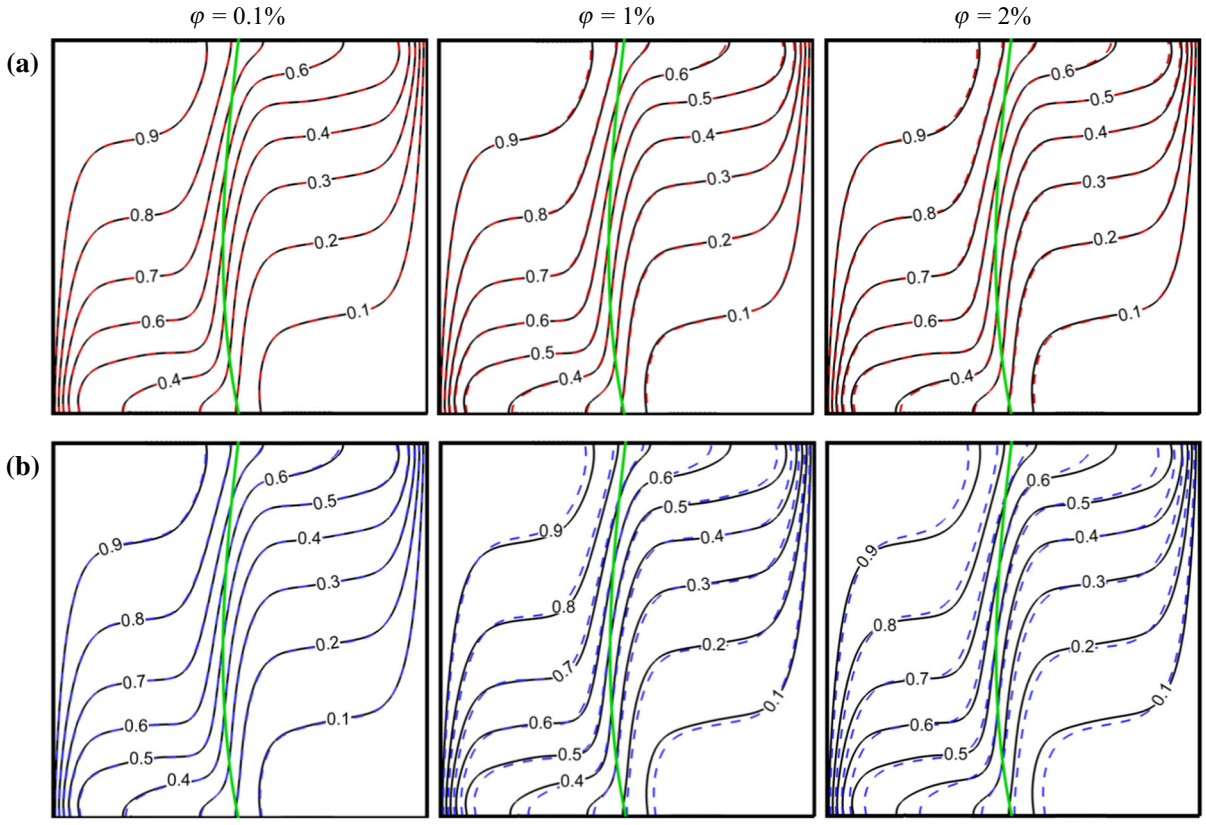

(I) $Ra = 10^6$

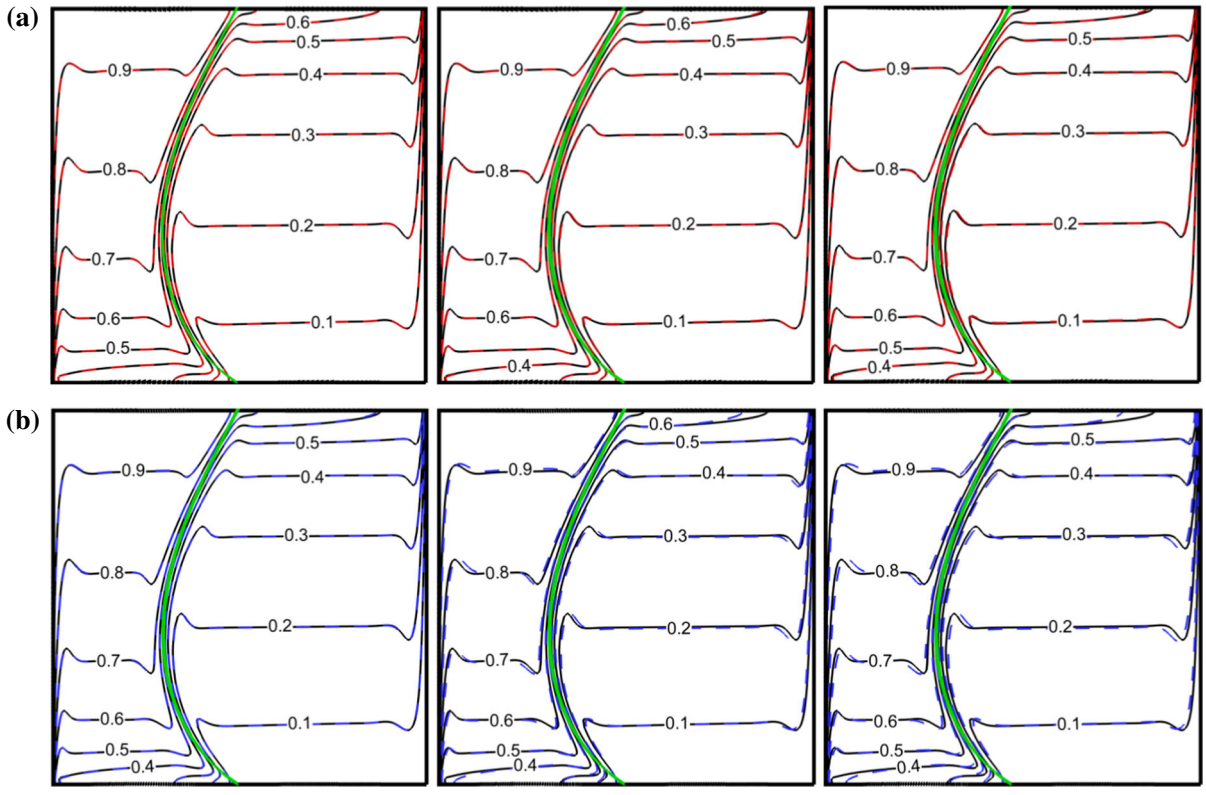

(II) $Ra = 10^8$

◀**Fig. 10** The isotherms contours of **a** Cu-Al_2O_3/water hybrid nanofluid (dashed lines) and **b** Al_2O_3/water nanofluid (dashed lines) for the various values of φ when **I** $Ra = 10^6$ and **II** $Ra = 10^8$ for the fixed values of $\gamma = 2\pi/3$ and $Ha = 50$

the amplitude of these quasi-sinusoidal functions increases with the increment of Ha. Figure 16a clearly indicates that the volume fraction 0.02 for Al_2O_3/water nanofluid causes increases in T_{avg} at all γ and Ha values. However, for Cu-Al_2O_3/water hybrid nanofluid adn $Ha = 200$, when $0 \leq$

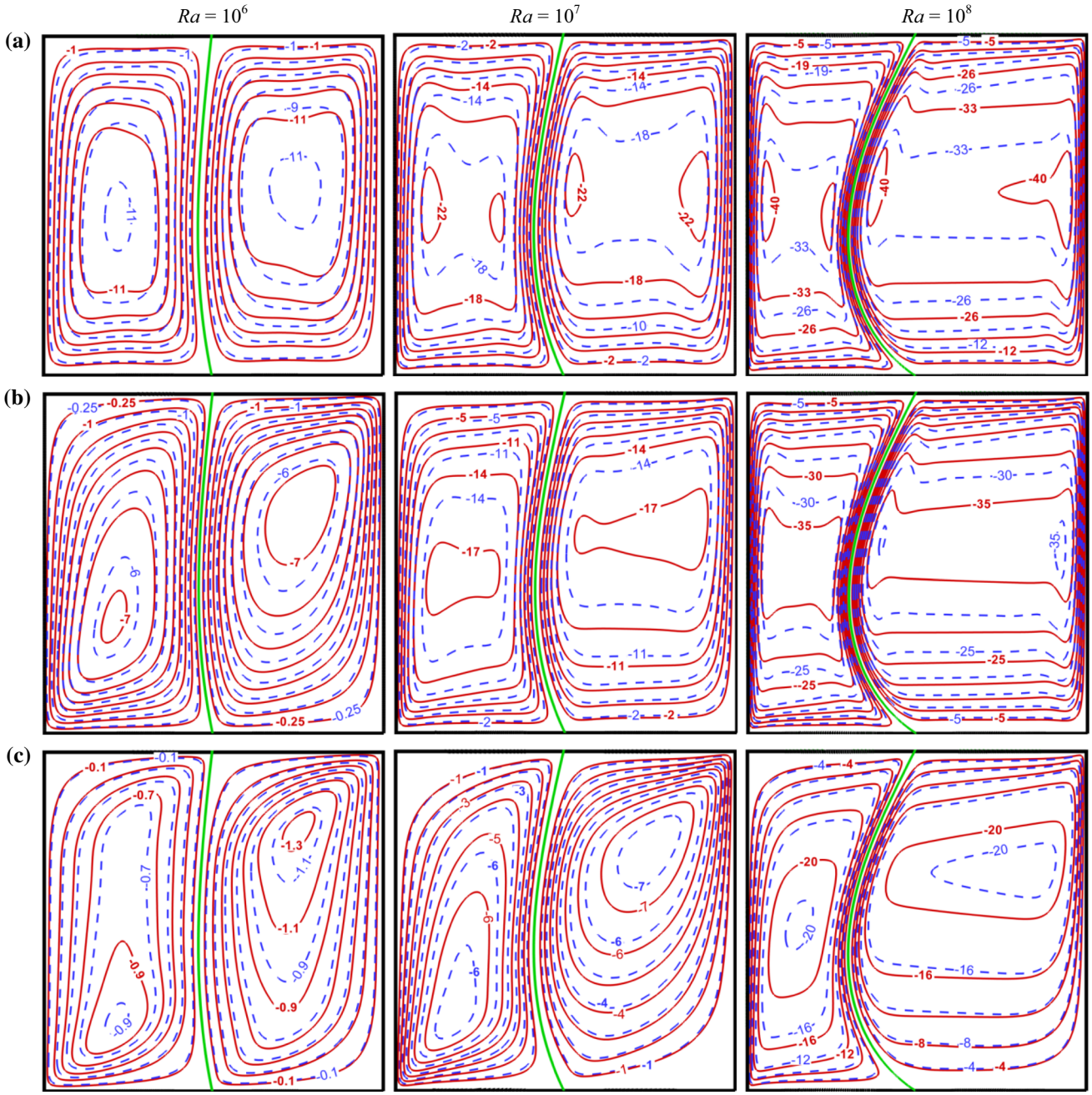

Fig. 11 The streamline contours of the hybrid nanofluid (dashed lines) and the nanofluid with Al_2O_3 nanoparticles (solid lines) for various values of Ra when **a** $Ha = 0$, **b** $Ha = 50$ and **c** $Ha = 200$ for $\gamma = \pi/6$ and $\varphi_{hnf} = \varphi_{Al_2O_3} = 2\%$

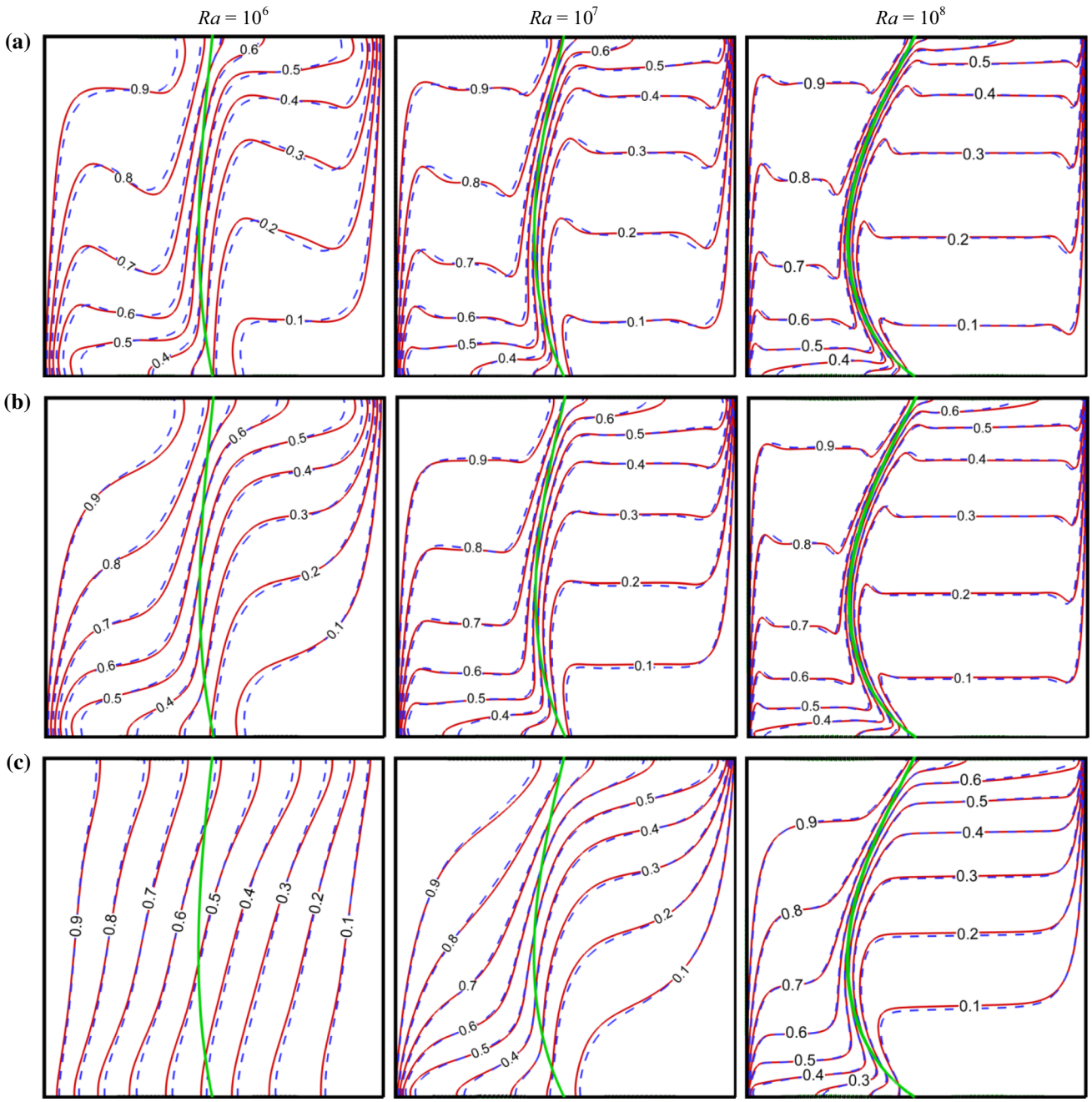

Fig. 12 The isotherms contours of the hybrid nanofluid (blue lines) and the nanofluid with Al_2O_3 nanoparticles (red lines) for the various values of Ra when **a** $Ha = 0$, **b** $Ha = 50$ and **c** $Ha = 200$ for $\gamma = \pi/6$ and $\varphi_{hnf} = \varphi_{Al_2O_3} = 2\%$. (Color figure online)

$\gamma < 120$ and $165 < \gamma \leq 180$, the simultaneous presence of Cu and Al_2O_3 raises T_{avg}. On the other hand, if $120 < \gamma < 165$, the presence of these nanoparticles decreases the mean temperature. Apparently, for all types of fluids, when $Ha = 100$ or 200, the maximum and minimum values of T_{avg} occurs at 50° and 140°, respectively.

Figure 17 illustrates that σ_{max} increases with an increase in Ha for all types of fluids. It is observed that at the beginning, σ_{max} decreases as γ increases by 30°. After that for $Ha \leq 100$, the maximum stress increases until γ reaches 105°, while for $Ha = 200$, the maximum stress occurs around $\gamma = 90°$. Then, it can be seen that σ_{max} continuously decreases as γ grows. Figure 17a, b expresses that the maximum stress imposed on the flexible partition due to the interaction of the pure fluid and the partition is

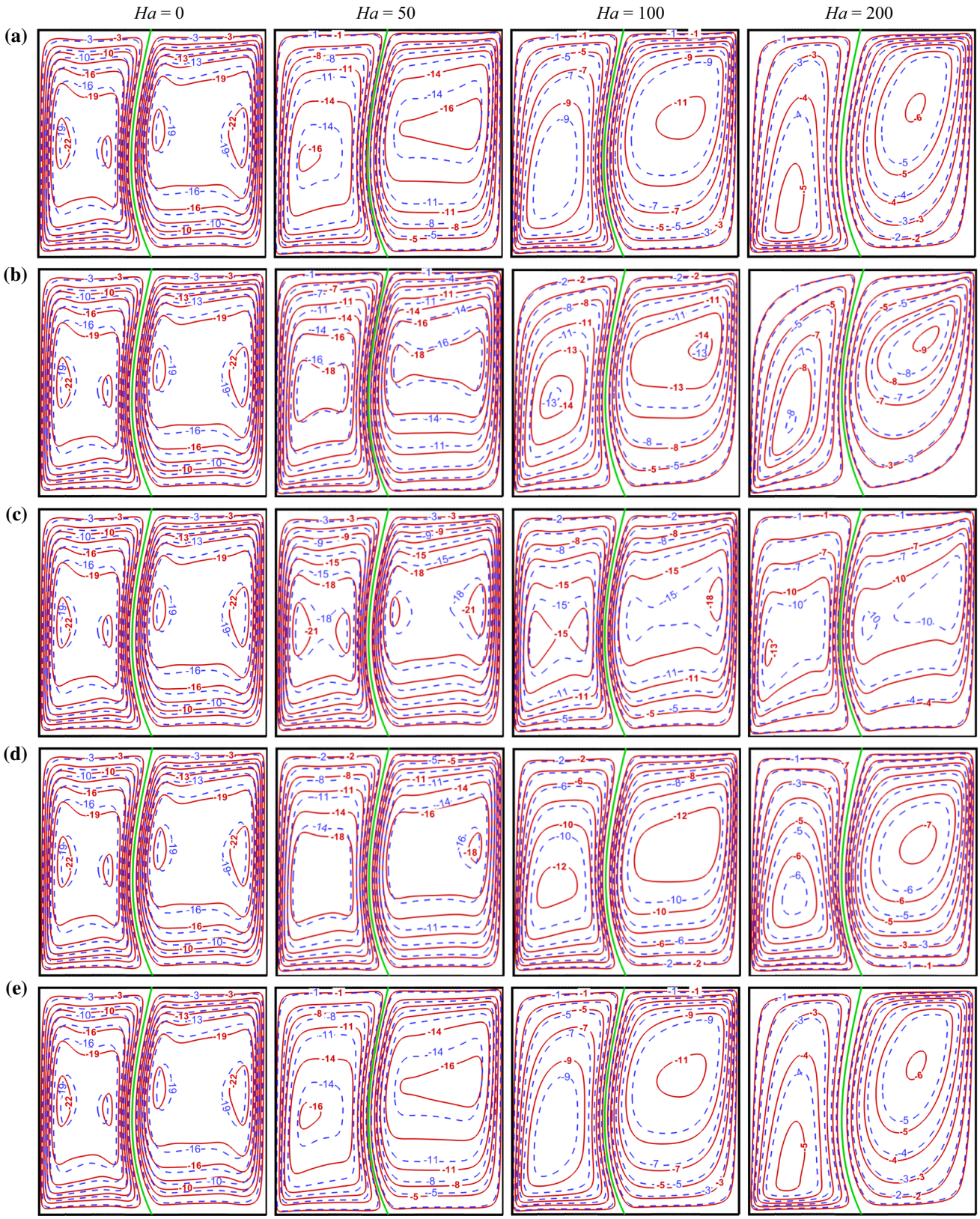

Fig. 13 The streamlines contours of the hybrid nanofluid (dashed lines) and the nanofluid with Al_2O_3 nanoparticles (solid lines) for different values of *Ha* in **a** $\gamma = 0$, **b** $\gamma = 45$, **c** $\gamma = 90$, **d** $\gamma = 135$ and **e** $\gamma = 180$ for $Ra = 10^7$ and $\varphi_{hnf} = \varphi_{Al_2O_3} = 2\%$

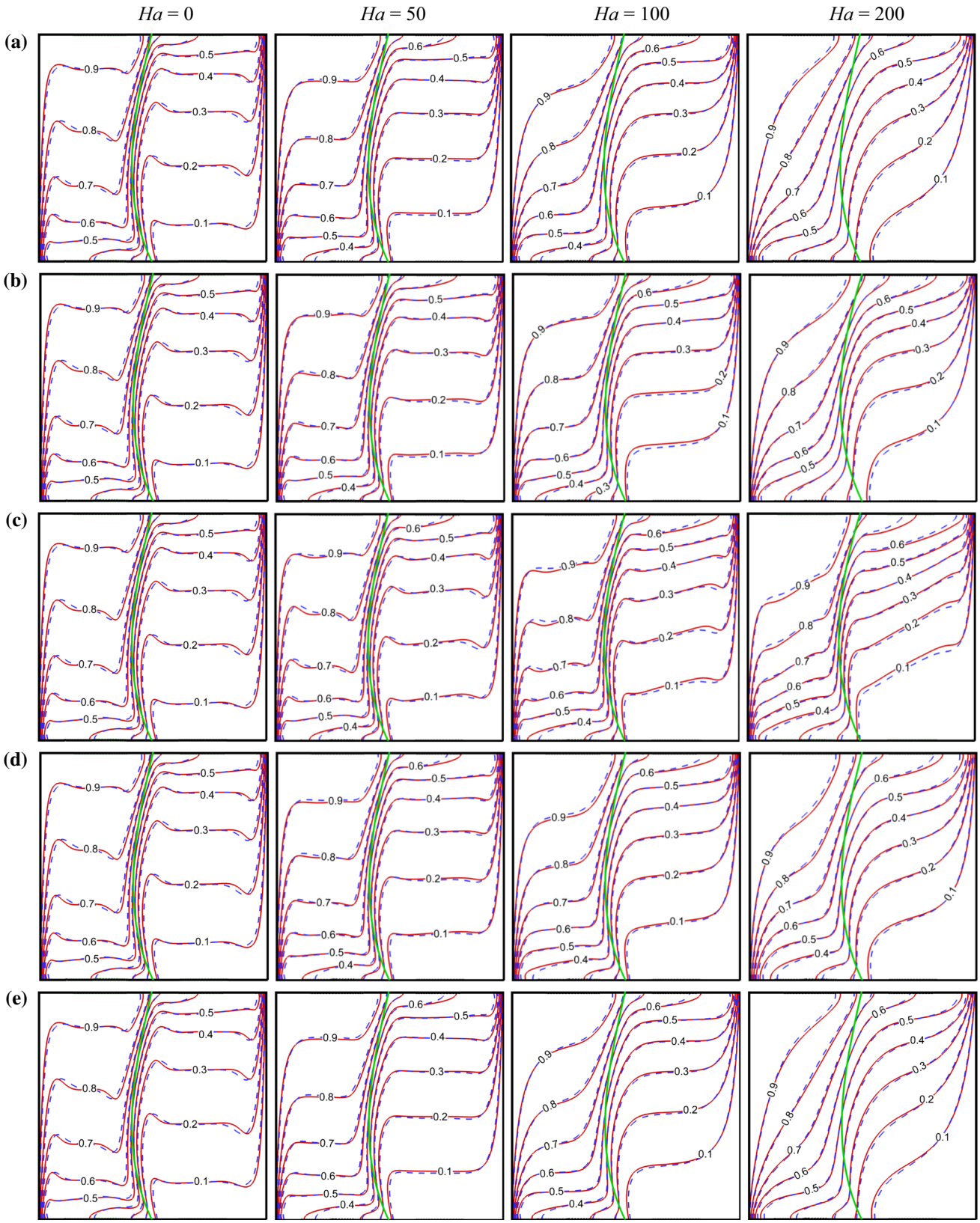

Fig. 14 The isotherms contours of the hybrid nanofluid (dashed lines) and the nanofluid with Al_2O_3 nanoparticles (solid lines) for different values of *Ha* in **a** $\gamma = 0$, **b** $\gamma = 45$, **c** $\gamma = 90$, **d** $\gamma = 135$ and **e** $\gamma = 180$ for $Ra = 10^7$ and $\varphi_{hnf} = \varphi_{Al_2O_3} = 2\%$

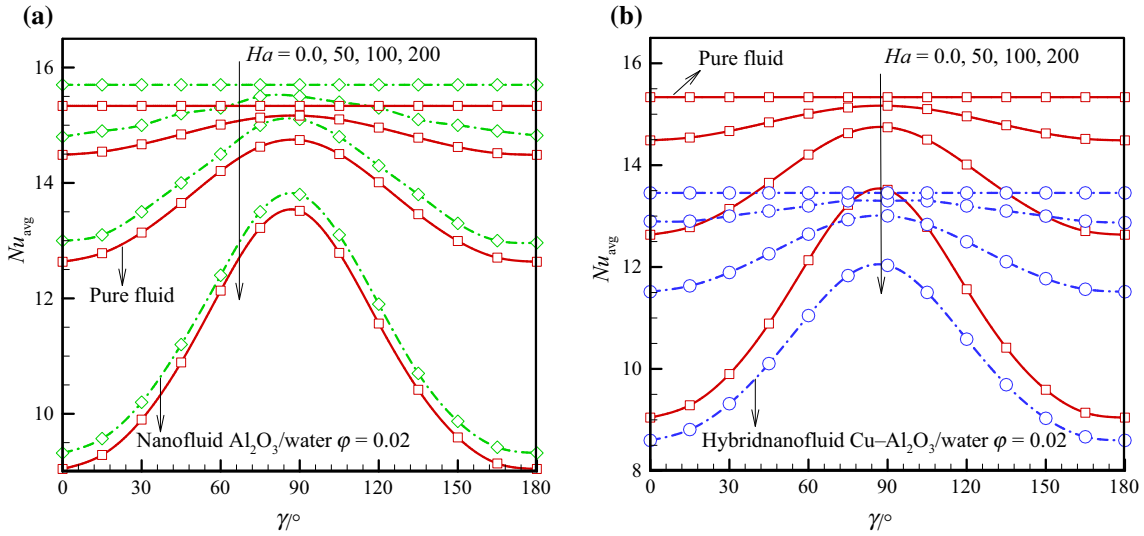

Fig. 15 The effects of Ha and γ on Nu_{avg} for **a** the nanofluid with $\varphi_{Al_2O_3} = 2\%$ and **b** the hybrid nanofluid with $\varphi_{hnf} = 2\%$ for $Ra = 10^8$

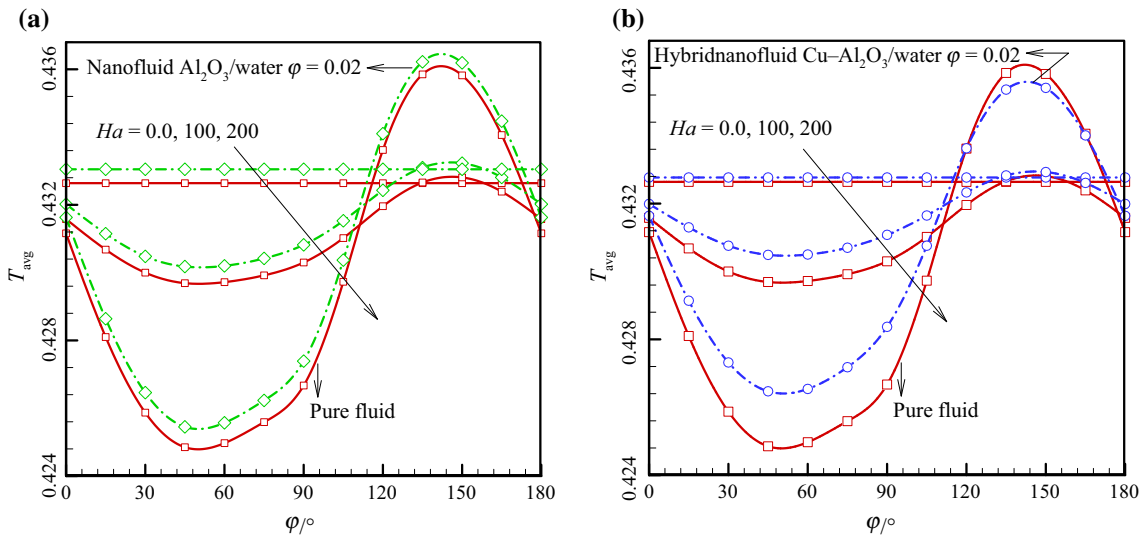

Fig. 16 The effects of Ha and γ on the average temperature T_{avg} for **a** the nanofluid with $\varphi_{Al_2O_3} = 2\%$ and **b** the hybrid nanofluid with $\varphi_{hnf} = 2\%$ for $Ra = 10^8$

more than that caused via the interaction of the nanofluid/hybrid nanofluid and the solid.

The effects of Ha and $\varphi_{hnf}/\varphi_{Al_2O_3}$ on Nu_{avg} and T_{avg} at the fixed values of $Ra = 10^7$ and $\gamma = 2\pi/3$ are presented in Fig. 18a, b. The examined values for the volume fractions are 1 and 2%. It is obvious that an increase in Ha increases and decreases the average temperature and Nusselt number, respectively. As previously mentioned, the magnetic field acts as a drag force against the fluid flow. Accordingly, increasing the value of Ha means augmentation in the drag force acting against the advection mechanism. In general, it can be said that for a specific volume fraction, the reduction in Nu_{avg} or augmentation of T_{avg} with increasing values of Ha for Al_2O_3/water nanofluid is more than that for Cu-Al_2O_3/water hybrid nanofluid. From Fig 18a, increasing the volume fraction of the single and hybrid nanofluids increases and decreases Nu_{avg}, respectively. In order to justify this outcome, it can be said that the increase in the hybrid nanofluid viscosity due to the simultaneous presence of Cu and Al_2O_3 nanoparticles is extremely larger than the increase in the other thermophysical properties especially the thermal conduction. Therefore, as previously seen, the intense reduction in the mobility of the hybrid nanofluid flow due to the intense increase in viscosity can

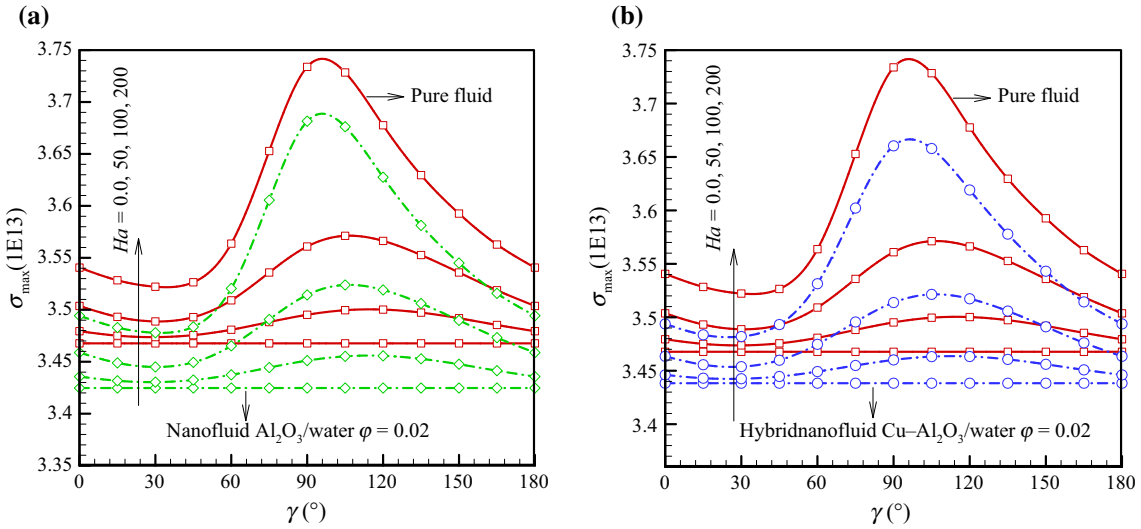

Fig. 17 The effects of Ha and γ on the maximum stress imposed on the partition for **a** the nanofluid with $\varphi_{Al_2O_3} = 2\%$ and **b** the hybrid nanofluid with $\varphi_{hnf} = 2\%$ for $Ra = 10^8$

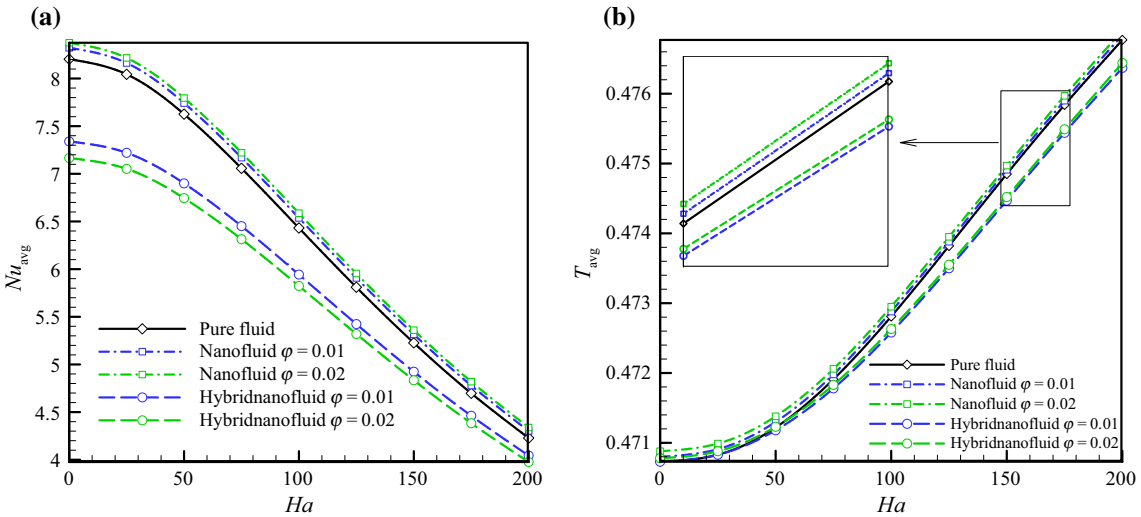

Fig. 18 The effects of Ha and φ on **a** the Nusselt number **b** the average temperature in $Ra = 10^7$, $\gamma = 2\pi/3$

be the reason of decreasing Nu_{avg}. Also, from Fig. 18b, it is concluded that the presence of Al_2O_3 and Cu–Al_2O_3 nanoparticles at $Ra = 10^7$ and $\gamma = 2\pi/3$ increases and decreases the average temperature of the fluid, respectively.

Figure 19 illustrates that for all types of fluids an increase in Ha increases σ_{max} when $Ra = 10^7$ and $\gamma = 2\pi/3$. On the other hand, the use of Al_2O_3 and Cu–Al_2O_3 nanoparticles decreases σ_{max}. Nevertheless, it cannot be said with certainty that which type of nanofluids reduce σ_{max} more. Generally, when $Ha \geq 100$ and for different values of φ, σ_{max} for the single and hybrid nanofluids are the same.

Comparison of Nu_{avg} of the single and hybrid nanofluids for different values of Ra and φ is presented in Table 4. The other parameters are selected constant so that $Ha = 50$ and $\gamma = \pi/3$. The data presented in Table 4 indicates that for all Ra values and both types of nanofluids, the Nu_{av} is decreased when $\varphi = 0.1$. Moreover, increasing the volume fraction of Al_2O_3 and Cu-Al_2O_3 nanoparticles enhances and declines the Nu_{avg}, respectively. The data also indicate that an increase in Ra extremely augments the heat transfer rate (Table 4).

The data presented in Table 5 give information on the mean temperature variations with Ra and φ when $Ha = 50$ and $\gamma = \pi/3$. Clearly, dispersing the single and hybrid nanoparticles in the host fluid increase T_{avg}. Moreover, the

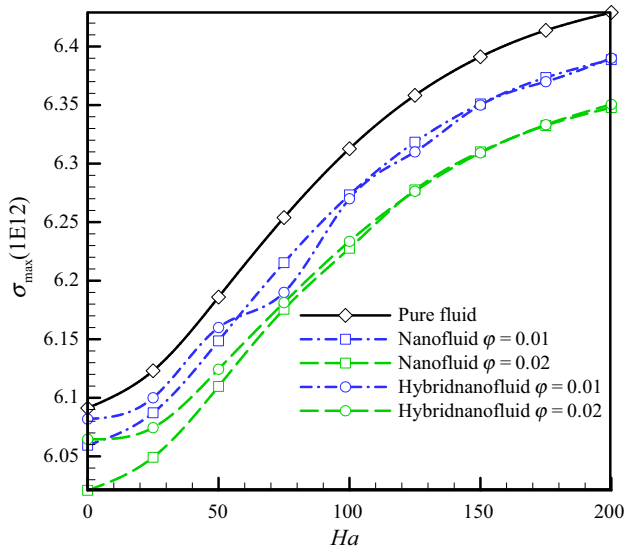

Fig. 19 The effects of Ha and φ on the maximum stress imposed on the partition at $Ra = 10^7$ and $\gamma = 2\pi/3$

results demonstrate that the increase in T_{avg} due to adding the hybrid nanoparticles is more than that for the single nanoparticles. Also, an increase in Ra extremely reduces T_{avg}.

The results given in Table 6 explain that at $Ha = 50$ and $\gamma = \pi/3$, the maximum stress in the flexible partition increases when Ra increases. In contrast, increasing the volume fraction of single and hybrid nanoparticles decreases the induced maximum stress. In fact, an increase in Ra makes an increase in the mobility of the fluid flow, consequently, increases the interaction between the fluid and solid. Also, comparison of the results shows that the maximum stress at the flexible partition of cavity filled with the hybrid nanofluid is more than that of cavity occupied using the single nanofluid.

Table 4 Comparison of Nu_{avg} of the single and hybrid nanofluids for various values of Ra and φ when $Ha = 50$ and $\gamma = \pi/3$

φ/%	$Ra = 10^6$		$Ra = 10^7$		$Ra = 10^8$	
	Al_2O_3/water	Cu–Al_2O_3/water	Al_2O_3/water	Cu–Al_2O_3/water	Al_2O_3/water	Cu–Al_2O_3/water
0.0	3.5920	3.5920	7.6867	7.6867	15.011	15.011
0.1	3.5827	3.5489	7.6631	7.5786	14.963	14.79
0.33	3.5991	3.4924	7.7002	7.4394	15.036	14.508
0.75	3.6367	3.374	7.7855	7.151	15.207	13.928
1	3.6479	3.2904	7.8045	6.9502	15.241	13.525
2	3.6741	3.2201	7.8579	6.7946	15.344	13.228

Table 5 Comparison of the average temperature between Al_2O_3/water nanofluid and Al_2O_3–Cu/water hybrid nanofluid for different values of Ra and φ

φ/%	$Ra = 10^6$		$Ra = 10^7$		$Ra = 10^8$	
	Al_2O_3/water	Cu–Al_2O_3/water	Al_2O_3/water	Cu–Al_2O_3/water	Al_2O_3/water	Cu–Al_2O_3/water
0.0	0.48600	0.48600	0.46966	0.46966	0.43180	0.43180
0.1	0.48601	0.48605	0.46968	0.4697	0.43182	0.43181
0.33	0.48603	0.48613	0.4697	0.46976	0.43187	0.43185
0.75	0.48606	0.48628	0.46973	0.46987	0.43195	0.43192
1	0.4861	0.48637	0.46977	0.46993	0.432	0.43196
2	0.48617	0.48653	0.46987	0.47004	0.43223	0.43213

Table 6 Comparison of the maximum value of stress in flexible partition between Al_2O_3/water nanofluid and Al_2O_3–Cu/water hybrid nanofluid for various values of Ra and φ when $Ha = 50$ and $\gamma = \pi/3$

φ/%	$Ra = 10^6$		$Ra = 10^7$		$Ra = 10^8$	
	Al_2O_3/water	Cu–Al_2O_3/water	Al_2O_3/water	Cu–Al_2O_3/water	Al_2O_3/water	Cu–Al_2O_3/water
0.0	1.1845E12	1.1845E12	6.1810E12	6.1810E12	3.4809E13	3.4809E13
0.1	1.1838E12	1.1839E12	6.1774E12	6.1703E12	3.4789E13	3.4800E13
0.33	1.1823E12	1.1826E12	6.1604E12	6.1648E12	3.4738E13	3.4768E13
0.75	1.1796E12	1.1802E12	6.1448E12	6.1544E12	3.4645E13	3.4712E13
1	1.1781E12	1.1788E12	6.146E12	6.1482E12	3.4597E13	3.4678E13
2	1.1713E12	1.1735E12	6.098E12	6.1352E12	3.4374E13	3.4493E13

Conclusions

Unsteady natural convection within an enclosure equally divided by a flexible partition is numerically investigated utilizing the Galerkin finite element method. The enclosure occupied by the hybrid nanofluid is under the influence of a uniform magnetic field. The effects of different parameters including the Hartmann number *Ha*, the Rayleigh number *Ra*, the nanoparticles concentration φ and the angle of the magnetic field vector γ on the flow strength, the rate of heat transfer and the stress of flexible partition are studied. The main findings of the current work are summarized as follows:

1. The strength of the hybrid and regular nanofluids circulation augments as the magnetic field vector angle γ increases until γ reaches $\pi/2$. Then, the mobility of fluid begins to vanish when γ varies from $\pi/2$ to π. The impact of magnetic field on the mean Nusselt number Nu_{avg} is the maximum at $\gamma = \pi/2$.
2. Compared to the base fluid, the presence of 2% volume fraction of Al_2O_3 nanoparticles increases Nu_{avg}, the same volume faction of Cu–Al_2O_3 nanoparticles decreases the average Nusselt number. Moreover, the presence of Al_2O_3 nanoparticles enhances the fluid flow strength while the combination of Cu and Al_2O_3 nanoparticles (hybrid nanoparticles) results in the reduction in circulation strength. The reduction in Nu_{avg} is mainly due to the significant increase in the dynamic viscosity of hybrid nanofluids.
3. The maximum stress imposed on the flexible partition coming from the pure fluid and the partition interaction is larger than that of the solid and regular/hybrid nanofluid interaction. The presence of nanoparticles would cause smaller partition deflection compared to the case of pure fluid.
4. The vortices-strength inside both the sub-cavities decreases with the increase of *Ha*. However, the fluid flow strength rises as *Ra* increases. Moreover, the dominant mechanism of heat transfer changes with *Ra* and *Ha* values. The presence of hybrid nanoparticles in the host fluid (water) results in a fluid with higher dynamic viscosity and thermal conductivity. The increase in the thermal conductivity tends to enhance the natural convective heat transfer; in contrast, the augmentation of the dynamic viscosity tends to decrease the heat transfer. The overall effect of dispersing hybrid nanoparticles in the host fluid is the reduction in Nu_{avg}. However, the presence of the same amount of single Al_2O_3 nanoparticles would enhance Nu_{avg}.

Acknowledgements This work was supported by the National Numerical Windtunnel (Grant 2018-ZT3A05) and 111 project of the Minstry of Science and Technology, China (No: B18002).

References

1. Ostrach S. Natural convection in enclosures. In: Hartnett JP, Irvine TF, editors. Advances in heat transfer, vol. 8. Hoboken: Elsevier; 1972. p. 161–227.
2. Sheikholeslami M, Soleimani S, Ganji DD. Effect of electric field on hydrothermal behavior of nanofluid in a complex geometry. J Mol Liq. 2016;213:153–61.
3. Al-Mudhaf AF, Chamkha AJ. Natural convection of liquid metals in an inclined enclosure in the presence of a magnetic field. Int J Fluid Mech Res. 2004;31(3):221–43.
4. Sheikholeslami M, Mehryan SAM, Shafee A, Sheremet MA. Variable magnetic forces impact on magnetizable hybrid nanofluid heat transfer through a circular cavity. J Mol Liq. 2019;277:388–96.
5. Chamkha AJ, Miroshnichenko IV, Sheremet MA. Numerical analysis of unsteady conjugate natural convection of hybrid water-based nanofluid in a semicircular cavity. J Therm Sci Eng Appl. 2017;9(4):041004-1–9.
6. Sathiyamoorthy M, Chamkha A. Effect of magnetic field on natural convection flow in a liquid gallium filled square cavity for linearly heated side wall (s). Int J Therm Sci. 2010;49(9):1856–65.
7. Sathiyamoorthy M, Chamkha AJ. Natural convection flow under magnetic field in a square cavity for uniformly (or) linearly heated adjacent walls. Int J Numer Methods Heat Fluid Flow. 2012;22(5):677–98.
8. Miroshnichenko IV, Sheremet MA, Oztop HF, Al-Salem K. MHD natural convection in a partially open trapezoidal cavity filled with a nanofluid. Int J Mech Sci. 2016;119:294–302.
9. Bondareva NS, Sheremet MA, Pop I. Magnetic field effect on the unsteady natural convection in a right-angle trapezoidal cavity filled with a nanofluid: Buongiorno's mathematical model. Int J Numer Methods Heat Fluid Flow. 2015;25(8):1924–46.
10. Gibanov NS, Sheremet MA, Oztop HF, Abu-Hamdeh N. Effect of uniform inclined magnetic field on mixed convection in a lid-driven cavity having a horizontal porous layer saturated with a ferrofluid. Int J Heat Mass Transf. 2017;114:1086–97.
11. Bahiraei M, Heshmatian S. Electronics cooling with nanofluids: a critical review. Energy Convers Manage. 2018;172:438–56.
12. Sheikholeslami M, Ganji DD. Nanofluid hydrothermal behavior in existence of Lorentz forces considering Joule heating effect. J Mol Liq. 2016;224:526–37.
13. Cheikh NB, Chamkha AJ, Beya BB. Effect of inclination on heat transfer and fluid flow in a finned enclosure filled with a dielectric liquid. Numer Heat Transf Part A Appl. 2009;56(3):286–300.
14. Chamkha AJ, Mansour M, Ahmed SE. Double-diffusive natural convection in inclined finned triangular porous enclosures in the presence of heat generation/absorption effects. Heat Mass Transf. 2010;46(7):757–68.
15. Chen KS, Ku AC, Chou CH. Investigation of natural convection in partially divided rectangular enclosures both with and without an opening in the partition plate: measurement results. J Heat Transf. 1990;112(3):648–52.
16. Bilgen E. Natural convection in enclosures with partial partitions. Renew Energy. 2002;26(2):257–70.
17. Dagtekin I, Oztop H. Natural convection heat transfer by heated partitions within enclosure. Int Commun Heat Mass Transf. 2001;28(6):823–34.

18. Nansteel M, Greif R. Natural convection in undivided and partially divided rectangular enclosures. J Heat Transf. 1981;103(4):623–9.
19. Nansteel MW, Greif R. An investigation of natural convection in enclosures with two- and three-dimensional partitions. Int J Heat Mass Transf. 1984;27(4):561–71.
20. Zargartalebi H, Ghalambaz M, Chamkha A, Pop I, Nezhad AS. Fluid-structure interaction analysis of buoyancy-driven fluid and heat transfer through an enclosure with a flexible thin partition. Int J Numer Methods Heat Fluid Flow. 2018;28(9):2072–88.
21. Jamesahar E, Ghalambaz M, Chamkha AJ. Fluid–solid interaction in natural convection heat transfer in a square cavity with a perfectly thermal-conductive flexible diagonal partition. Int J Heat Mass Transf. 2016;100:303–19.
22. Mehryan S, Chamkha A, Ismael M, Ghalambaz M. Fluid–structure interaction analysis of free convection in an inclined square cavity partitioned by a flexible impermeable membrane with sinusoidal temperature heating. Meccanica. 2017;52(11–12):2685–703.
23. Mehryan S, Ghalambaz M, Ismael MA, Chamkha AJ. Analysis of fluid-solid interaction in MHD natural convection in a square cavity equally partitioned by a vertical flexible membrane. J Magn Magn Mater. 2017;424:161–73.
24. Xu F, Patterson JC, Lei C. Heat transfer through coupled thermal boundary layers induced by a suddenly generated temperature difference. Int J Heat Mass Transf. 2009;52(21):4966–75.
25. Nishimura T, Shiraishi M, Nagasawa F, Kawamura Y. Natural convection heat transfer in enclosures with multiple vertical partitions. Int J Heat Mass Transf. 1988;31(8):1679–86.
26. Oztop HF, Varol Y, Koca A. Natural convection in a vertically divided square enclosure by a solid partition into air and water regions. Int J Heat Mass Transf. 2009;52(25):5909–21.
27. Kahveci K. Natural convection in a partitioned vertical enclosure heated with a uniform heat flux. J Heat Transf. 2007;129(6):717–26.
28. Ramezanizadeh M, Alhuyi Nazari M, Ahmadi MH, Açıkkalp E. Application of nanofluids in thermosyphons: a review. J Mol Liq. 2018;272:395–402.
29. Mahian O, Kianifar A, Kalogirou SA, Pop I, Wongwises S. A review of the applications of nanofluids in solar energy. Int J Heat Mass Transf. 2013;57(2):582–94.
30. Kasaeian A, et al. Nanofluid flow and heat transfer in porous media: a review of the latest developments. Int J Heat Mass Transf. 2017;107:778–91.
31. Chamkha AJ, Molana M, Rahnama A, Ghadami F. On the nanofluids applications in microchannels: a comprehensive review. Powder Technol. 2018;332:287–322.
32. Tahmasebi A, Mahdavi M, Ghalambaz M. Local thermal nonequilibrium conjugate natural convection heat transfer of nanofluids in a cavity partially filled with porous media using Buongiorno's model. Numer Heat Transf Part A Appl. 2018;73(4):254–76.
33. Mehryan S, Ghalambaz M, Izadi M. Conjugate natural convection of nanofluids inside an enclosure filled by three layers of solid, porous medium and free nanofluid using Buongiorno's and local thermal non-equilibrium models. J Therm Anal Calorim. 2019;135(2):1047–67.
34. Kahveci K. Buoyancy driven heat transfer of nanofluids in a tilted enclosure. J Heat Transf. 2010;132(6):062501.
35. Jena P, Brocchi E, Motta M. In-situ formation of Cu–Al_2O_3 nanoscale composites by chemical routes and studies on their microstructures. Mater Sci Eng A. 2001;313(1–2):180–6.
36. Suresh S, Venkitaraj K, Selvakumar P, Chandrasekar M. Synthesis of Al_2O_3–Cu/water hybrid nanofluids using two step method and its thermo physical properties. Colloids Surf A. 2011;388(1–3):41–8.
37. Suresh S, Venkitaraj K, Selvakumar P, Chandrasekar M. Effect of Al_2O_3–Cu/water hybrid nanofluid in heat transfer. Exp Thermal Fluid Sci. 2012;38:54–60.
38. Mahian O, et al. Recent advances in modeling and simulation of nanofluid flows—part I: fundamental and theory. Phys Rep. 2019;790:1–48.
39. Mahian O, et al. Recent advances in modeling and simulation of nanofluid flows—part II: applications. Phys Rep. 2019;791:1–59.
40. Izadi M, Mohebbi R, Karimi D, Sheremet MA. Numerical simulation of natural convection heat transfer inside a$^{\perp}$ shaped cavity filled by a MWCNT-Fe_3O_4/water hybrid nanofluids using LBM. Chem Eng Process Process Intensif. 2018;125:56–66.
41. Mehryan S, Sheremet MA, Soltani M, Izadi M. Natural convection of magnetic hybrid nanofluid inside a double-porous medium using two-equation energy model. J Mol Liq. 2019;277:959–70.
42. Mehryan S, Kashkooli FM, Ghalambaz M, Chamkha AJ. Free convection of hybrid Al_2O_3–Cu water nanofluid in a differentially heated porous cavity. Adv Powder Technol. 2017;28(9):2295–305.
43. Ghalambaz M, Doostani A, Izadpanahi E, Chamkha A. Phase-change heat transfer in a cavity heated from below: the effect of utilizing single or hybrid nanoparticles as additives. J Taiwan Inst Chem Eng. 2017;72:104–15.
44. Chamkha A, Doostanidezfuli A, Izadpanahi E, Ghalambaz M. Phase-change heat transfer of single/hybrid nanoparticles-enhanced phase-change materials over a heated horizontal cylinder confined in a square cavity. Adv Powder Technol. 2017;28(2):385–97.
45. Ghalambaz M, Doostani A, Chamkha AJ, Ismael MA. Melting of nanoparticles-enhanced phase-change materials in an enclosure: effect of hybrid nanoparticles. Int J Mech Sci. 2017;134:85–97.
46. Mehryan SAM, Izadpanahi E, Ghalambaz M, Chamkha AJ. Mixed convection flow caused by an oscillating cylinder in a square cavity filled with Cu–Al_2O_3/water hybrid nanofluid. J Therm Anal Calorim. 2019. https://doi.org/10.1007/s10973-019-08012-2.
47. Alsabery A, Sheremet M, Ghalambaz M, Chamkha A, Hashim I. Fluid-structure interaction in natural convection heat transfer in an oblique cavity with a flexible oscillating fin and partial heating. Appl Therm Eng. 2018;145:80–97.
48. Maxwell JC, Thompson JJ. A treatise on electricity and magnetism. Oxford: Clarendon Press; 1904.
49. Murshed SMS, Leong KC, Yang C. Enhanced thermal conductivity of TiO_2–water based nanofluids. Int J Therm Sci. 2005;44(4):367–73.
50. Einstein A. Investigations on the theory of the brownian movement. North Chelmsford: Courier Corporation; 1956.
51. Brinkman H. The viscosity of concentrated suspensions and solutions. J Chem Phys. 1952;20(4):571.
52. Batchelor G. The effect of Brownian motion on the bulk stress in a suspension of spherical particles. J Fluid Mech. 1977;83(1):97–117.
53. Küttler U, Wall WA. Fixed-point fluid–structure interaction solvers with dynamic relaxation. Comput Mech. 2008;43(1):61–72.
54. Churchill SW. Free convection in layers and enclosures. In: Heat exchanger design handbook, vol. 2, no. 8, 1983.